

JULIUS-MAXIMILIANS-UNIVERSITÄT WÜRZBURG

BACHELOR'S THESIS

**Spectral Analysis of *Swift*-XRT
monitoring observations of the blazar Mrk
501**

Author:
Jonas Sinapius



*A thesis submitted in fulfillment of the requirements
for the degree of Bachelor of Science*

Lehrstuhl für Astronomie

July 14, 2017

“Es gibt nur eine Landstraße der Wissenschaft, und nur diejenigen haben Aussicht ihren hellen Gipfel zu erreichen, die die Ermüdung beim Erklettern ihrer steilen Pfade nicht scheuen.”

Karl Marx

Julius-Maximilians-Universität Würzburg

Abstract

Fakultät für Physik und Astronomie
Lehrstuhl für Astronomie

Bachelor of Science

Spectral Analysis of *Swift*-XRT monitoring observations of the blazar Mrk 501

by Jonas Sinapius

Active Galactic Nuclei (AGN) are some of the most exciting cosmological objects known to us. As they emit intense radiation over the whole electromagnetic spectrum, they can be observed in multiwavelength campaigns, making use of the advantages of different telescopes. One special case of AGN are the so called blazars, emitting a relativistic particle jet pointed towards earth which produces intense radiation. While the physics behind the jets are not yet understood, the fact that blazars show spectral variability on all timescales offers a way to learn more about the processes responsible for the building and flaring of a jet. A BL Lac blazar's spectral energy distribution (SED) typically shows two bumps. The lower energetic one can be attributed to electron-synchrotron emission, but the origin of the high energy peak is still a matter of debate. The Würzburg Blazar Monitoring program's goal is to observe a blazar before, during and after an outburst over multiple bands, the sample includes Mrk 501 and Mrk 421, two well studied BL Lac objects. Therefore, in this work, the X-ray spectrum of the high energy peaked BL-Lac blazar Mrk 501 is examined over a two year period, using data taken by the *Swift*-XRT during 2015 and 2016. The data was then fit using a log-parabolic model (Massaro et al., 2004). While Mrk 501 becomes fainter over the course of the two years, it also exhibits moderate fractional variability of about 37 %. Also, the comparison of the photon index α with the flux, both derived from spectral fitting, showed the many times observed *harder when brighter* trend (Connolly et al., 2015), meaning blazars often harden their spectrum during periods of higher fluxes, a trend that can also be seen using only model-independent data, namely the count rate and the hardness ratio (HR). The origin of this trend is not understood, and in this work, it has been found during a low flux state, instead of only during flaring activity. During the chosen period, the source was in a declining, quiescent state, especially when compared with data from e.g. 2009 (Acciari et al., 2011). This gives a excellent baseline for the further investigation of this source, as it enables us to compare any flare detected to its quiescent state and thus quantify its intensity. With the ongoing of this campaign and other similar programs, it is only a matter of time until different jet-emission models can be compared using a large sample of sources imaged in different energy bands, and then ruled out or supported by the data taken.

Julius-Maximilians-Universität Würzburg

Abstract

Fakultät für Physik und Astronomie
Lehrstuhl für Astronomie

Bachelor of Science

Spectral Analysis of *Swift*-XRT monitoring observations of the blazar Mrk 501

by Jonas Sinapius

Aktive Galaxienkerne (AGN) gehören zu den aufregendsten kosmologischen Objekten, die uns bekannt sind. Da sie im ganzen elektromagnetischen Spektrum intensiv strahlen, können sie unter Ausnutzung der Vorteile verschiedenster Teleskope im Rahmen von Multiwellenlängenkampagnen beobachtet werden. Ein Spezialfall von AGN sind die sogenannten Blazare, die sich durch die Emission eines Jets relativistischer Teilchen in Richtung Erde, der starke Strahlung produziert, auszeichnen. Während die physikalische Ursache dieser Jets noch nicht bekannt ist, eröffnet die spektrale Variabilität, die Blazare auf allen Zeitskalen zeigen, einen Weg, die Prozesse, die verantwortlich für Entstehung und Flackern der Jets sind, zu verstehen. Die spektrale Energieverteilung (SED) eines BL-Lac Blazars weist typischerweise zwei Höcker auf. Der niederenergetische Höcker kann durch Elektron-Synchrotronstrahlung erklärt werden, die Ursache des bei höheren Energien liegenden lokalen Maximums ist ein Streitthema. Das Ziel des Würzburg Blazar Monitoring Programms ist es, einen Blazar vor, während und nach einem Ausbruch in verschiedenen Energiebändern zu beobachten. Das Sample enthält die zwei viel erforschten BL-Lac Objekte Mrk 501 und Mrk 421. In dieser Arbeit wird daher das Röntgenspektrum von Mrk 501, aufgenommen von *Swift*-XRT in den Jahren 2015 und 2016 analysiert. Die Daten wurden mit einem log-parabolischen Modell (Massaro et al., 2004) gefittet. Im Laufe der zwei Jahre wird Mrk 501 dunkler, und zeigt moderate fraktionale Variabilität bei einem Wert von ca. 37 %. Der Vergleich des Photonindex α mit dem Fluss, zwei Größen erhalten aus dem spektralen Fit, zeigt den oft beobachteten *harder when brighter* Trend (Connolly et al., 2015), der bedeutet, dass Blazare in Phasen höheren Flusses zugleich oft das Spektrum zu höheren Energien verschieben. Dieser Trend kann bereits bei der Analyse modellunabhängiger Daten, nämlich der Zählrate und der Hardness Ratio (HR) gesehen werden. Der Ursprung dieses Trends ist nicht bekannt. Im Rahmen dieser Arbeit wurde der Trend während einer Phase niedrigen Flusses beobachtet, anstatt nur bei Ausbrüchen aufzutreten. Während des Zeitfensters von zwei Jahren befand sich Mrk 501 in einem ruhigen, abnehmenden Zustand, besonders im Vergleich zu Daten von z.B. 2009 (Acciari et al., 2011). Damit bietet diese Arbeit eine gute Basislinie für weitere Beobachtungen dieser Quelle, da sie uns ermöglicht, entdeckte Ausbrüche mit dem ruhigen Zustand zu vergleichen, und somit deren Intensität zu quantifizieren. Mit dem Fortschreiten dieses, und anderer, ähnlicher Programme, ist es nur eine Frage der Zeit, bis verschiedene Jet-Emissions Modelle anhand von großen Quellsamples in verschiedenen Energiebereichen verglichen und anhand der Beobachtungsdaten angenommen oder abgelehnt werden können.

Contents

Abstract	ii
1 Introduction	1
2 Scientific Background	2
2.1 AGN	2
2.1.1 Properties	2
2.1.2 Classification	2
2.1.3 Model and Unification	5
2.2 Blazars	7
3 Markaryan 501	9
3.1 Motivation	9
3.2 Properties	9
4 The <i>Swift</i> Telescope	11
4.1 Goal	11
4.2 The XRT	11
4.2.1 Technical data and functionality	11
4.2.2 Constraints and Inaccuracies	12
4.2.3 Imaging modes	13
5 Methods and spectral modeling	15
5.1 Phenomenological computations	15
5.2 Modelfitting	15
5.3 Models used	15
5.4 Flux variability	16
6 Data Analysis	17
6.1 Swift Data	17
6.2 Data extraction	19
6.3 Pile-up	20
6.4 Background reduced data	20
6.5 Data processing	21
7 Data evaluation	23
7.1 Phenomenological spectral Analysis	23
7.2 Evaluation of the logpar model	23
7.3 Discussion	25
7.4 Conclusion	27
A Appendix	28
Bibliography	32

Acknowledgements	36
Declaration of Authorship	37

List of Figures

2.1	Radio image of 3C 272.1, a typical Fanaroff-Riley 1 galaxy. (Laing and Bridle, 1987)	4
2.2	Radio image of the quasar 3C 175 with FR2 morphology. Image courtesy of NRAO/AUI.	4
2.3	Unification model according to Urry and Padovani (1995). Note that an AGN as displayed in this image does not exist, as one side is radio loud and the other radio quiet. This has been done in order to include all types in one image.	5
2.4	Optical spectra of different AGN types. Different line widths in type 1 and 2 can be seen, as well as the typical flat BL-Lac spectrum. (<i>Optical spectra of various kinds of active galactic nuclei</i>)	7
2.5	Spectral energy distribution (SED) of the blazar Mrk 501, using all available data. The two bumps can be distinguished, as well as the high variability, which is about two orders of magnitude around the synchrotron peak. (Image produced via http://tools.asdc.asi.it/)	8
3.1	SED of Mrk 501 over a wide energy range. The TeV emission can be seen as well as the synchrotron peak in the X-ray band. The image was taken from Aleksić et al. (2015).	10
4.1	Diagram of the <i>Swift</i> -XRT. Image taken from (Burrows et al., 2005).	12
4.2	The XRT's CCD energy resolution, image taken from (Burrows et al., 2005).	13
6.1	The number of observations over the respective source counts. 5 observations had less than 100 source counts total and are therefore ignored in the fitting process, as not enough bins with the required size are available to use χ^2 statistics.	20
6.2	Exemplary spectrum of observation 00092205011 with residuals in the lower panel. The <i>logpar</i> model fits the data very well, $\chi_{red}^2 = 1.0135$	22
7.1	The Hardness Ratio HR over time in MJD. A weak declining trend can be seen, indicating a softening of the spectrum over time.	23
7.2	The count rate over time in MJD. The count rate seems to decrease as a function of time.	24
7.3	The χ_{red}^2 values for each observation, plotted over the time axis. The values scatter around the optimal reduced χ^2 of 1.	24
7.4	The curvature parameter β of the <i>logpar</i> model over time. Mean value and one standard deviation to both sides are plotted to illustrate the constancy of β	25
7.5	The photon index α from the <i>logpar</i> model plotted over time. Mean value and standard deviation are included to better visualize the trend of a rising α as a function of time.	25

7.6	The flux computed with the model <i>cflux</i> over time. Mean value and standard deviation underline the declining of the flux during the two years.	26
7.7	Photon index α plotted over the flux. Higher fluxes seem to show lower photon indices and vice versa. This is a strong indication of the <i>harder when brighter</i> trend. A linear regression line is drawn to better illustrate this behavior.	26

List of Tables

2.1	The different AGN types divided in radio loud and radio quiet. Adapted from M. Kadler.	6
4.1	Technical data of the <i>Swift</i> -XRT. Table adapted from (<i>Swift XRT data</i>). .	12
6.1	ObsIDs of all <i>Swift</i> -XRT observations of Mrk 501 in 2015 and 2016. . . .	17
A.1	All best-fit parameter values and errors for the convolution of <i>logpar</i> with <i>cflux</i>	28

Chapter 1

Introduction

The information for this chapter was taken from the book 'A brief history of AGN' by Gregory A. Shields. The fact that so called Active Galactic Nuclei (AGN) emit intense luminosities over a wide spectrum, and that the origin of this radiation is a very small region at the center of galaxies makes them an excellent natural laboratory to study physics in extreme conditions. Their extraordinary brightness allows us to observe them even at large redshifts, making AGN the main source of information when studying the formation and evolution of the early universe. When Fath (1909) tried to understand the nature of spiral nebulae, he found evidence for both theses, namely stellar absorption lines and bright lines as previously found in gaseous nebula. The large width of those lines indicated a Doppler broadening due to rapid movement of the absorbing medium, first quantified by Seyfert (1943). As, back at the beginning of the 20th century, only optical telescopes were really available, just this limited part of the electromagnetic spectrum could be measured. Only with the rise of radio astronomy during the 1950s did the research on AGN gain more popularity in the astronomic society. Cooperations between optical and radio astronomers lead to more precise localization and identification of radio sources as known optical sources. Over the years, observation techniques became more sophisticated, radio astronomy yielded better resolution and, one after the other, more wavelength bands could be examined. X-ray astronomy became relevant in the 1960s when observations could be made above the earth's atmosphere with rockets, balloons and later on, satellites. The same goes for γ -ray astronomy, as most of the high energetic radiation is absorbed in the atmosphere, but with the difference that since the late 1980s, ground based γ -ray observations are possible using the Cherenkov effect. Nowadays, AGN are among the most studied astronomical objects and are observed over the whole accessible range of the electromagnetic spectrum, extending from long-wavelength radio detection to multiple TeV γ -rays. Due to the great advance in the study of extragalactic objects over the last decades, physicists now have a deeper understanding in the mechanisms of AGN, but many questions remain unanswered, and theories unproven, as for example about the exact mechanisms which lead to the formation of jets, or their composition. These details are not yet understood, but profound knowledge on this is fundamental in order to precisely describe the physics happening inside AGN.

Chapter 2

Scientific Background

2.1 AGN

In this theory chapter, general properties as well as different types and a unification scheme of AGN are introduced. If not noted differently, the information in this chapter is based on Krolik (1999).

2.1.1 Properties

A galactic nucleus is considered active, when its emission is of non-thermal origin, meaning the stars that form the galaxy are not the major source of radiation, but instead a very luminous core exhibits broadband emission. Usual luminosities are in the range from 10^{42} to 10^{47} erg s⁻¹ (e.g. Peterson et al., 2004), emitted in all spectral bands from radio to γ -ray energies. Masses range from about 10^7 to $10^{10} M_{\odot}$ (e.g. Vestergaard and Peterson, 2006). Another important property of AGN is their flux as well as spectral variability, occurring on both short (minutes to hours) and large (months to years) timescales. In some AGN, a twin outflow of collimated, relativistic matter originating from the core perpendicular to the accretion disk can be seen. These phenomena are referred to as jets. Their orientation towards the line of sight can cause Doppler boosting, making them appear brighter if oriented towards the observer and fainter if pointed away from earth, often making it hard to find the counterjet if it's pointing away.

2.1.2 Classification

Depending on the matter of interest, AGN can be classified according to different schemata. A convenient way to distinguish them is to divide them into two classes: radio-loud and radio-quiet. The radio loudness was defined as the ratio between radio-flux at 5 GHz and the flux in optical (B) band: $R = L_{\nu}(5GHz)/L_{\nu}(B)$ (Kellermann et al., 1989) and a division line between radio loud and radio quiet was drawn at a value of $R = 10$, even though radio loud AGN can reach values $R > 100$. Radio-quiet AGN are typically missing visible jets, as in those radio-quiet jets no relativistic boosting happens and energy is not radiated away efficiently. Furthermore, as only some AGN show broad emission lines in the optical spectrum, they can generally be divided in Type 1 and Type 2 objects, where Type 1 shows broad and narrow optical lines and Type 2 only exhibits narrow line optical emission. These narrow lines are often 'forbidden' lines, meaning they occur with a much lower probability than 'allowed' lines. Their occurrence indicates that the material responsible for their emission must have lower densities so that these unlikely state transitions can happen undisturbed by particle collision or other interactions. Other classification

schemes introduce different names for AGN with different properties, mostly in the optic waveband:

- Seyfert galaxies (Seyfert, 1943) of type 1 and 2 (depending on the visible optic lines), that are located in spiral galaxies and are radio quiet. Their X-ray emission is over a hundred times more intense than their radio emission.
- LINER (Low-Ionization Nuclear Emission Line Region) galaxies with an optical spectrum similar to Seyfert 2 galaxies, but with a weaker continuum.
- Quasars (Quasi Stellar Radio Sources) or QSOs (Quasi Stellar Objects), which, due to their high redshift, mostly can not be associated with an optical source (their host galaxy). QSOs are usually radio quiet and can be divided in type 1 and 2 depending on the emission lines. Again, the optical spectrum is very similar to the one seen in Seyfert Galaxies. Their radio loud counterparts are named Flat Spectrum Radio Quasars (FSRQ), which make up only about a tenth of the QSO population.
- Radio galaxies, that are subdivided in Broad Line Radio Galaxies (BLRG) and Narrow Line Radio Galaxies (NLRG). They are usually observed in elliptical galaxies, but can, apart from that, be seen as the radio loud counterparts of Seyfert galaxies.
- Fanaroff-Riley galaxies (Fanaroff and Riley, 1974), a morphological classification of radio loud AGN in two types (FR1 & FR2): FR1 are core-dominated AGN with two symmetric jets ending in plumes, while FR2 are more luminous, jet-lobe-dominated objects that often only show one weak jet ending in radio lobes. See Figs. 2.1 and 2.2 for visualization.
- Blazars are further classified in Optically Violent Variables (OVVs), BL Lac Objects (the name is derived from BL Lacertae, an AGN originally classified as a star due to the absence of emission lines) and FSRQs (Flat Spectrum Radio Quasars), which are more luminous than BL Lac and show emission lines like QSOs. These objects are radio loud and are among the most luminous AGN, while emitting a variable non-thermal broadband spectrum.

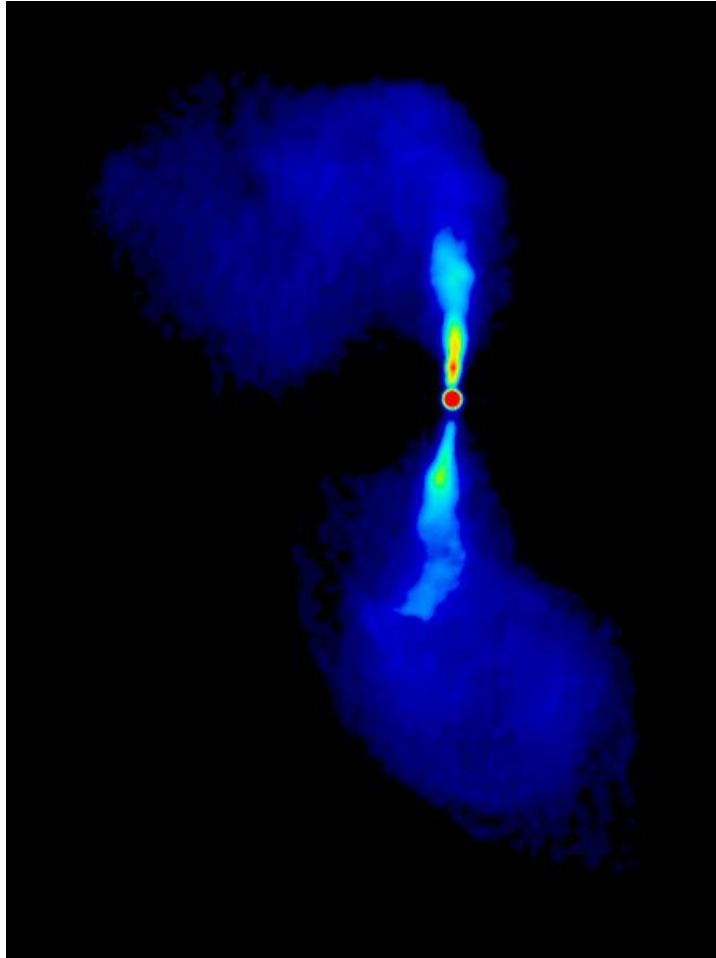


FIGURE 2.1: Radio image of 3C 272.1, a typical Fanaroff-Riley 1 galaxy. (Laing and Bridle, 1987)

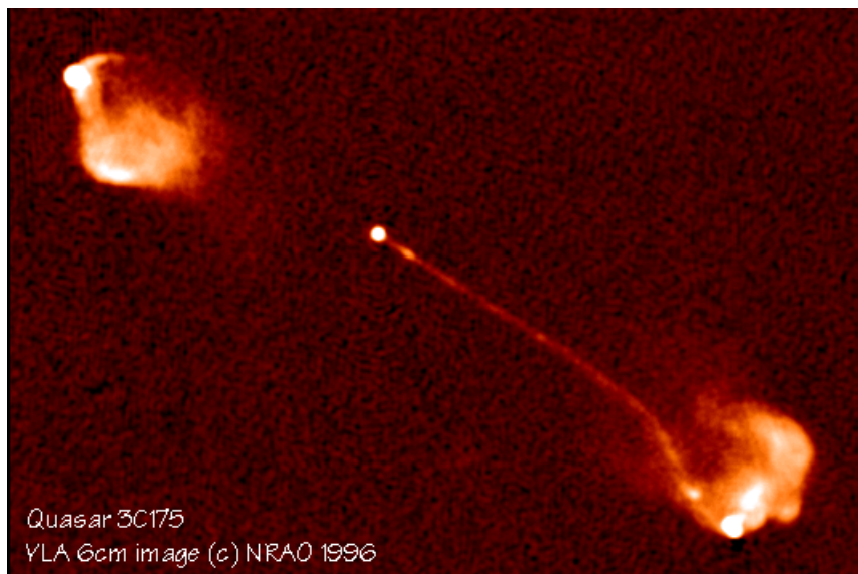


FIGURE 2.2: Radio image of the quasar 3C 175 with FR2 morphology. Image courtesy of NRAO/AUI.

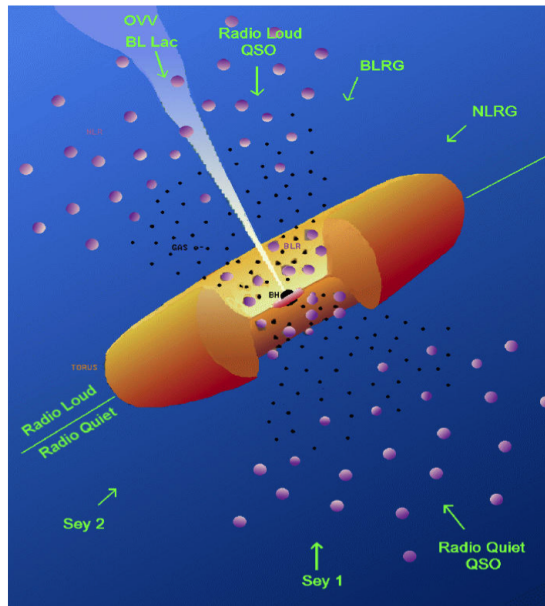


FIGURE 2.3: Unification model according to Urry and Padovani (1995). Note that an AGN as displayed in this image does not exist, as one side is radio loud and the other radio quiet. This has been done in order to include all types in one image.

2.1.3 Model and Unification

The generally accepted model for AGN, the so called standard model (see e.g. Urry and Padovani (1995) or Antonucci (1993)), puts a supermassive black hole with masses ranging from 10^7 to 10^{10} Solar Masses (Vestergaard and Peterson, 2006) in the center of a galaxy, which accretes matter, forming an accretion disk rotating at high velocities. This accretion process can explain the immense energy outflow measured in AGN. While an accretion spectrum itself is a thermal spectrum, the reflection, absorption and re-emission reshape it to the observed non-thermal spectrum that can be described by a power law. As will be explained later on, depending on the classification of the source, emission and absorption lines can be found in some AGN, the broadening of which can yield information on the rotational velocity of the absorbing matter. Furthermore, these lines are redshifted due to cosmic expansion, and can therefore be used to determine the distance of the object in question. The typical constituents of an AGN are described more precisely in the following, a schematic visualization of this model is given in Fig. 2.3.

- An angular-momentum dominated flow of matter towards the central black hole forms an accretion disc at a sub-parsec scale. The gas in this disc gets heated up by friction and compression and cools by thermal radiation.
- For some AGN the accretion process produces highly collimated, twin outflows of matter at relativistic velocities along the axis of rotation of the disc (jets). These jets are a very prominent feature in the radio band and can reach lengths of hundreds of kiloparsec (see e.g. Figs. 2.1 and 2.2).
- The broad line region (BLR) is a region around the central black hole, where dust-free clouds of gas are in Keplerian motion around said black hole. This

region is typically up to a parsec in size. Because of their high speeds, these clouds are the source of broad emission lines, hence their name.

- A torus around the central engine is composed mainly of dust, with dimensions ranging from 0.01 to 10 parsec. Previously it was thought to be quite homogeneous, yet more recent studies suggest a more clumpy composition (e.g. Elitzur, 2006).
- The narrow line region (NLR), located further away from the black hole, is composed of lower density ionized gas, which can reach up to thousands of parsec out from the central black hole. Due to lower velocities, the emission lines are narrower, thus the name.

This AGN model suggests that, depending on the orientation of the observed object, different characteristics can arise. As Antonucci (1993) proposed and Urry and Padovani (1995) supported, one can assume that the different known types of AGN are actually the same class of object and that the different properties can be explained by the observer's viewing angle. Fig. 2.3 shows a simple model including the different AGN regions and explaining the types mentioned above by orientation. The classification in types 1 and 2, discriminating between AGN showing narrow and broad lines and those showing only narrow lines, would thus be only an effect of the dust torus obscuring the accretion disk and therefore the BLR in some AGN, while others are viewed under such an angle that the BLR can be seen directly. This idea was first brought forward by Rowan-Robinson (1977). While the line-dependent classification seems to be an alignment effect, the difference between radio loud and radio quiet AGN is an intrinsic one, as only the radio loud population shows relativistic radio jets. But again, the different types of radio loud AGN (FR 1 & 2, FSRQ, Blazars) can be explained based on the inclination angle. Where blazars are observed under a very small angle between the line of sight and the jet, FR galaxies are essentially the same object, just rotated by about 90° . As the directly observed jet in blazars is Doppler boosted, the counterjet is mostly hard to see due to its lower brightness, but in FR galaxies no Doppler boosting happens in the jet, so that both jets are equally observable. In Table 2.1, the different types and their properties are shown and Fig. 2.4 shows typical, optical spectra of different AGN classes.

Type	Radio Loudness	Emission Lines	Luminosity	Jets	Radio Morphology
Sy 1	RQ	B & N	Low	-	-
Sy 2	RQ	N	Low	-	-
QSO(type 1)	RQ	B & N	High	-	-
QSO(type 2)	RQ	N	High	-	-
BLRG	RL	B & N	Low	Yes	FR 1
	RL	B & N	High	Yes	FR 2
NLRG	RL	N	Low	Yes	FR 1
	RL	N	High	Yes	FR 2
BL Lac	RL	-	Low	Yes	Compact
FSRQ	RL	B & N	High	Yes	Compact

TABLE 2.1: The different AGN types divided in radio loud and radio quiet. Adapted from M. Kadler.

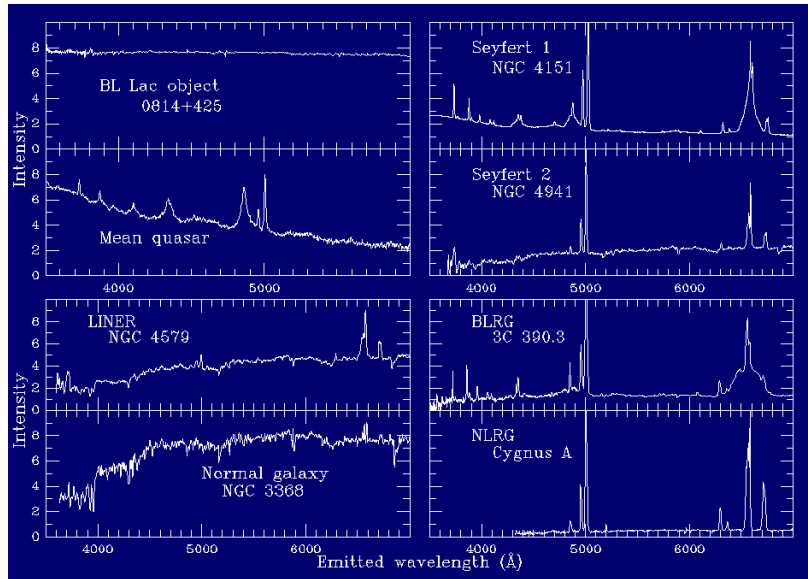


FIGURE 2.4: Optical spectra of different AGN types. Different line widths in type 1 and 2 can be seen, as well as the typical flat BL-Lac spectrum. (*Optical spectra of various kinds of active galactic nuclei*)

Even though this unification model is a very nice way to explain different phenomena, it is still an oversimplification of a larger context. For example, an exact division line between radio loud and radio quiet objects is simply not there. Radio quiet AGN also show radio emission, they usually do not emit jets, or at least none that can be observed with today's techniques. Another problem is the precise classification of blazar objects, BL Lacs and FSRQs are sometimes hard to tell apart, depending on the intensity of the FSRQ's lines.

2.2 Blazars

As this thesis deals with one object only, namely the blazar Mrk 501, this subclass of AGN will be discussed in more detail. The studies done by EGRET, a γ -ray telescope on board the *Compton Gamma-ray Observatory (CGRO)* detected many blazars emitting at energies greater than 30 MeV and found that a substantial part of their overall emission happens in the γ -band. A blazar's Spectral Energy Distribution (SED) shows two prominent bumps, one in the hard UV or soft X-ray band, and one in the hard X-ray to γ -ray regime (Donato et al., 2001). An example SED of a blazar can be seen in Fig 2.5.

Whereas it is generally accepted that the low-energy continuum (radio to UV/soft X-ray) of blazars can be traced back to synchrotron emission in a relativistic jet, the origin of their very high energy (VHE) emission is still widely disputed. O'Dell et al. (1978) first predicted a VHE component due to an inverse-compton upscattering of low-energy photons. The photons in question could be produced by the accretion disk, or upscattered in the BLR (e.g. Ghisellini and Madau, 1996). Another explanation is the so-called SSC (synchrotron-self-compton) model, attributing the γ -emission to the synchrotron photons themselves, being upscattered by the same lepton population that produces the synchrotron radiation (e.g. Bloom et al., 1993). Apart from these leptonic models, hadronic scenarios are also plausible, in which ultrarelativistic protons are responsible for the γ -outflow in blazars via different

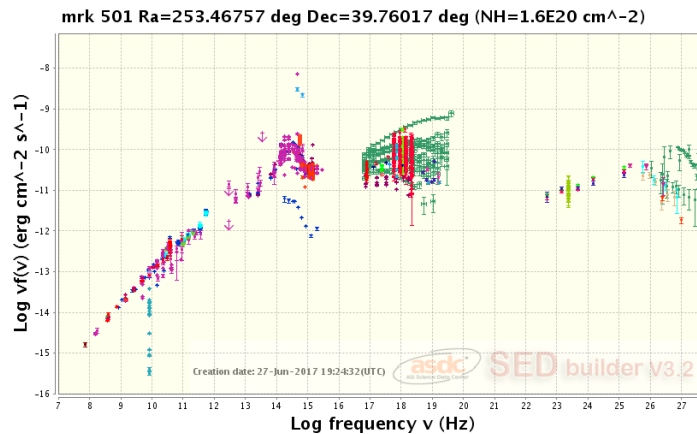


FIGURE 2.5: Spectral energy distribution (SED) of the blazar Mrk 501, using all available data. The two bumps can be distinguished, as well as the high variability, which is about two orders of magnitude around the synchrotron peak. (Image produced via <http://tools.asdc.asi.it/>)

mechanisms like proton-synchrotron emission or electromagnetic cascades from the decay of secondary particles as π -mesons (see e.g. Mannheim 1993 and references therein). Depending on the energy of the synchrotron peak, BL Lac blazars can be divided in different classes, namely high- (HBL) intermediate- (IBL) and low-energy (LBL) peaked blazars (e.g. Fossati et al., 1998). HBL show their synchrotron bump at energies in the hard UV to soft X-ray band, while LBL peak in the IR-regime and IBL in the optical to soft UV regime (Abdo et al., 2010). In addition, the position of the high energy peak seems to depend on the synchrotron peak, following the same relation. HBL blazars, as Mrk 501, have been discovered with Cherenkov telescopes such as H.E.S.S. and MAGIC (e.g. Cologna et al., 2015). Therefore, X-ray astronomy is a great way to study the synchrotron peak in HBL objects, while the high energy peak can be observed simultaneously via Cherenkov astronomy. Possible correlation (or anti-correlation) in the light curves in the two energy-bands could support or rule out the models mentioned, so that multiwavelength observations of blazars are a good possibility to finally understand how AGN jets are produced and what they are composed of.

Chapter 3

Markaryan 501

3.1 Motivation

The goal of the Würzburg Blazar Monitoring Program is to gain time-resolved multiwavelength spectra of flaring blazars with *target of opportunity* observations of the two objects Mrk 501 and Mrk 421. With this information, different radiation models can be compared and evaluated better as the variability observed during a flare in different energy bands can yield constraints on radiative processes (Weidinger, R uger, and Spanier, 2010). To gain multiwavelength data of flaring AGN, a continuous TeV γ -ray monitoring is performed by FACT; X-ray and optical data of the cooldown after a bright TeV flare triggering the observations are collected by the *INTEGRAL – Swift* program. Additionally, via the *Swift* program, snapshots from the X-ray, UV and optical bands are taken on a weekly basis during the visibility windows in order to gain pre- and post flare information, which can then be used to differentiate between orphan flares and innerband timelags. As the Blazar Mrk 501 is part of this sample, I will analyze the X-ray data from all *Swift* observations of the object taken in 2015 and 2016.

3.2 Properties

The blazar Mrk 501, named after its discoverer Benjamin Markaryan, was first studied in 1974 during a study on galaxies with excessive UV-emission. When first detected, its continuous spectrum led the researchers to classify the object as a BL Lac object (Markaryan and Lipovetskii, 1972). Mrk 501 lies in the Hercules constellation, in an elliptical host galaxy, with a right ascension of 16 h 53.9 m and a declination of 39° 45' and its redshift determined to 0.033663 ± 0.000073 (Vaucouleurs et al., 1991), the object therefore being one of the nearest blazars detected. In 1965, during the Fourth Cambridge Survey (4C), Mrk 501 was found to produce radio emission and to possess a radio-jet. Only in more recent years its striking VHE emission was discovered. In 1996, Mrk 501 was determined to be the brightest TeV source known during a phase of high emission (Quinn et al., 1996). Then, in 2005, Mrk 501 was observed with MAGIC Telescope at energies above 100 GeV and significant short time variability was detected, flux-doubling times as low as 2 minutes were observed (Albert et al., 2007). Again, in 2014, the AGN was observed by the H.E.S.S. telescope and short time variability at very high energies was discovered (Chakraborty et al., 2015). Mrk 501 has been known to undergo both short time and long time variability (e.g. Catanese et al. (1997); Pian et al. (1998); Albert et al. (2007)), primarily in the keV to VHE range.

The two bumps in the SED mentioned in Sect. 2.2 and shown in Fig. 3.1 have been

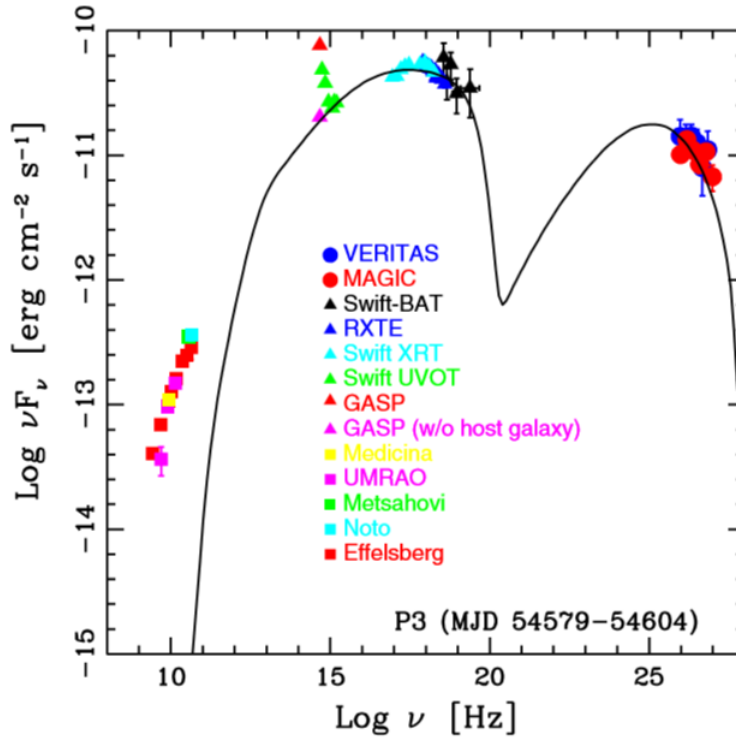


FIGURE 3.1: SED of Mrk 501 over a wide energy range. The TeV emission can be seen as well as the synchrotron peak in the X-ray band. The image was taken from Aleksić et al. (2015).

observed to move towards higher energies during phases of increased brightness, essentially hardening the observed spectrum (Connolly et al., 2015). This phenomenon is often referred to as the *harder when brighter* trend, meaning sources like Mrk 501 tend to harden its spectrum when outbursts occur (Pian et al., 1998). In this thesis, it is examined whether there was variability in the spectrum during the chosen time interval. If so, γ -ray data may be used to compare changes in both bands to evaluate e.g. the SSC-model. Mrk 501, with its high luminosity making it easy to observe, thus makes for a very interesting target for the study on variability in Blazar emission, and possibly also on the final understanding of jet mechanisms. As it is one of the most prominent and intensely studied VHE objects, much information on other studies and earlier results can be found (e.g.: Acciari et al. (2011), Albert et al. (2007), Ahnen et al. (2016)).

Chapter 4

The *Swift* Telescope

4.1 Goal

The *Swift* Telescope (Gehrels et al., 2004) was launched in November 2004 by NASA, with the aim to permit real-time multiwavelength observations of gamma-ray bursts (GRBs) and their afterglow. One main goal of the mission is to understand the origin and mechanism of these GRBs, and to gain more information about the early universe with that knowledge, as most of these high-energetic outbursts are detected at cosmological distances. Between GRB events, *Swift* is used for other research done by universities and other scientific institutions. Besides, the *Swift* mission performs an all-sky survey to improve the catalog of known X-ray sources. The spacecraft is therefore equipped with a burst alert telescope (BAT) (Barthelmy et al., 2005), which recognizes and then locates GRBs, and an X-ray telescope (XRT), which can point at detected GRBs within 100 s and localize them with a precision of up to a few arcseconds (Burrows et al., 2005). *Swift* also carries an ultraviolet/optical telescope (UVOT) (Roming et al., 2005) to observe the optical afterglow, and which can reach sub-arcsecond positioning precision. Within seconds, the location of the GRB is transmitted to ground-based observatories that can then observe the afterglow. As this thesis is about X-ray observations of an AGN, which only uses XRT data, this chapter will focus on *Swift*'s XRT instead of going into further detail on the other instruments.

4.2 The XRT

4.2.1 Technical data and functionality

The following main requirements were set on the XRT: The ability to determine the position of a source precisely and rapidly and to create highly time-resolved light curves. In order to do so, the *Swift* XRT uses a Wolter I X-ray telescope with 12 mirrors to focus the X-rays onto a MOS CCD chip, yielding an effective area of 110 cm², a 15 arcsec resolution over a 23.6 · 23.6 arcmin² field of view and an energy range from 0.2 to 10 keV, with a resolution of 140 eV at 6 keV. The CCD, which was originally designed for the *XMM-Newton* satellite, is based on the photodiode principle. Incoming X-rays interact with the silicon atoms, leading to both electron- and hole current, which is proportional to the detected photon's energy. The CCD has an imaging area of about 2.4 · 2.4 cm (Burrows et al., 2005). All technical data on the *Swift*-XRT can be found summarized in Table 4.1, a schematic diagram of the telescope is shown in Fig. 4.1.

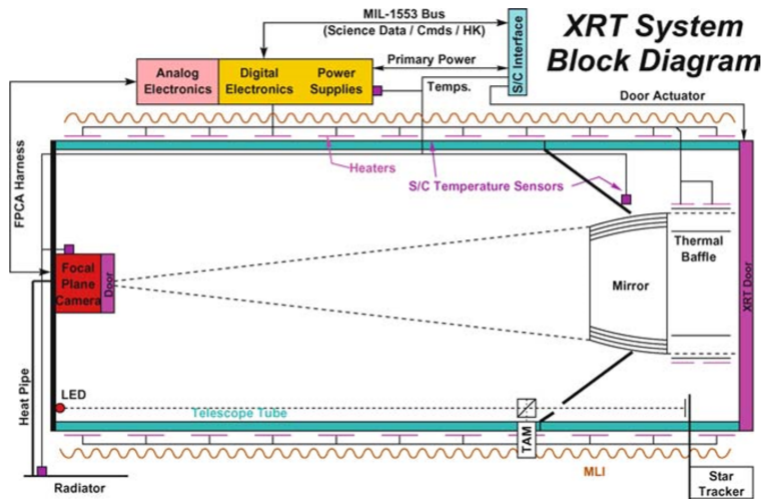


FIGURE 4.1: Diagram of the *Swift*-XRT. Image taken from (Burrows et al., 2005).

Property	Description
Telescope	JET-X Wolter I
Focal Length	3.5 m
Effective Area	110 cm ² @ 1.5 keV
Detector	EEV CCD-22, 600 x 600 pixels
Detector Operation	Imaging, Timing and Photon-counting
Detection Element	40 x 40 micron pixels
Pixel Scale	2.36 arcsec/pixel
Energy Range	0.2 - 10 keV
Sensitivity	4 x 10 ⁻¹⁴ erg cm ⁻² s ⁻¹ in 10 ⁴ seconds for known sources 1 x 10 ⁻¹³ erg cm ⁻² s ⁻¹ in 10 ⁴ seconds for blind searches

TABLE 4.1: Technical data of the *Swift*-XRT. Table adapted from (*Swift XRT data*).

4.2.2 Constraints and Inaccuracies

To avoid optical light pollution, the CCD is protected by a thin filter, coated in aluminum on one side. If the telescope points towards the sun at angles below 30 degrees, the XRT is shut down, if the angle becomes lower than 10 degrees, a shutter is closed in front of the opening to protect the instruments. The CCD's energy resolution is shown in Fig. 4.2. One can easily see that the accuracy decreases for lower energies. At energies under 0.5 keV charge trapping effects and the loss of surface states lead to a significantly lower energy resolution, which is why all data below 0.5 keV was excluded in the analysis. A CCD's quantum efficiency (QE) depends on the depletion depth at high energies and the gate structure for lower frequencies. The open-gate electron structure leads to a high low energy QE, whereas the high resistivity silicon gives the chip a good QE at higher energies.

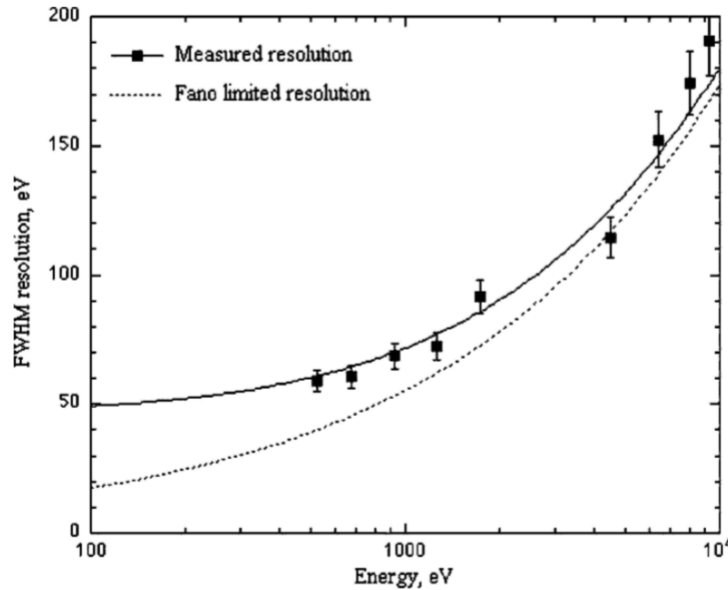


FIGURE 4.2: The XRT's CCD energy resolution, image taken from (Burrows et al., 2005).

4.2.3 Imaging modes

The X-ray telescope on board the *Swift* spacecraft can operate in four different modes, always autonomously selecting the most accurate one. When a new target is chosen, the XRT first records data in Imaging Mode in order to determine the target's location. Depending on the detected count rate, one of the other modes Photodiode, Windowed Timing and Photon Counting is chosen automatically. The different modes will be explained in detail in the following, with information taken from Burrows et al. (2005):

1. Imaging Mode (im): Imaging Mode is used to detect sources and give a first constraint on its localization. Therefore, it works like an optical CCD with a variable exposure time, currently 0.1 and 2.5 seconds. The on board software does not correct for pile-up, but observations in Imaging Mode can yield good flux and position estimates.
2. Photodiode Mode (pd): This mode uses fast timing to produce light curves with high time resolution and can be used for fluxes below 60 Crab¹. For fluxes below 2 Crab, pile-up can be reasonably corrected for. Above 3 Crab, the spectroscopic information suffers significant losses. pd mode offers no spatial information but has full energy resolution. The Photodiode Mode has been turned off after the impact of a micrometeoroid in 2005.
3. Windowed Timing Mode (wt): wt produces 1-D images with a millisecond time resolution and full energy resolution. In wt mode, pile-up does not occur below fluxes of about 0.1 Crab and is useful for fluxes up to 5 Crab. Only the central 200 columns, which is equal to about 8 arcmin, are read out.
4. Photon Counting Mode (pc): While pc mode yields full 2-D imaging and spectral resolution, its time resolution is rather low with only 2.5 seconds. This mode is only used at fluxes below 1 mCrab.

¹Flux of the Crab nebula: 815,781,667.2 counts s⁻¹ for the *Swift*-XRT (Kirsch et al., 2005)

The flux limits were taken from Burrows et al. (2005) and Romano et al. (2006) respectively.

Chapter 5

Methods and spectral modeling

5.1 Phenomenological computations

In order to describe an AGN's X-ray properties without choosing a model, the hardness ratio HR can be computed after the fractional difference method (Park et al., 2006) via

$$HR = \frac{H - S}{H + S} \quad (5.1)$$

HR is the hardness ratio, H are the source counts in the hard band, ranging from 2 to 10 keV and S are the source counts in the 0.5 to 2 keV soft band. For a hard spectrum, in which more counts are measured in the hard band, the hardness ratio would be a positive value, while a soft spectrum would yield a negative hardness ratio. The phenomenological source count rate can be computed by dividing the number of source counts by the observation's respective exposure time.

5.2 Modelfitting

To evaluate the source's intrinsic spectrum, one has to make certain assumptions depending on the model used. Generally, when trying to fit a model to experimental data, it has to be examined statistically. One method that can be used is χ^2 statistics. This statistic model can be written as follows for m observations:

$$\chi^2 = \sum_{j=1}^m \frac{(N_j - n_{0j})^2}{n_{0j}} \quad (5.2)$$

N_j is the observed occurrence and n_{0j} the expected occurrence for a certain null-hypothesis. A large deviation from the expectation, resulting in large χ^2 values, indicates the assumed distribution does not describe the data well, while for smaller χ^2 the model fits the data better. Furthermore, taking into account the degrees of freedom (DOF), a reduced χ^2 can be computed by dividing χ^2 by the DOF. A χ^2_{red} of 1 indicates a perfect fit. By applying this statistic, the model parameters are varied until the resulting χ^2 value reaches a minimum. While χ^2 statistics assume normal distribution and the observed counts are naturally Poisson distributed, a larger event rate is needed for the Poisson distribution to converge towards a normal distribution.

5.3 Models used

To describe the overall shape of the taken data, a log-parabolic model is chosen. This *logpar* model has been shown by Massaro et al. (2004) to model nonthermal

high energy spectra better than simple powerlaws (see also Cusumano et al. (2001)). The *logpar* model can be written as

$$N(E) = A(E/E_p)^{-\alpha-\beta\log(E/E_p)} \quad (5.3)$$

, where E is the energy in keV, E_p the pivot energy, which is frozen to 1 keV, α is the photon index at E_p , β is the curvature and A is the normalization factor. To account for absorption, the *tbnew_simple* model is used, describing X-ray absorption in the interstellar medium using only one parameter, which is the hydrogen column density n_H . This *tbnew_simple* model makes use of the *Verner* cross section (Verner et al., 1996) to describe the non-relativistic photoionization cross sections for the ground states of different atoms and ions and the element abundance (Wilms, Allen, and McCray, 2000) to account for X-ray absorption in the interstellar medium. The convolution model *cflux* is used to obtain the unabsorbed flux of the *logpar* model in the 0.5 - 10 keV band.

5.4 Flux variability

A way to determine the variability amplitude for n measurements, taking into account the symmetrized measurement errors, is the fractional variability method (Vaughan et al., 2003):

$$F_{var} = \sqrt{\frac{S^2 - \langle \sigma_{err}^2 \rangle}{\langle F_\gamma \rangle^2}} \quad (5.4)$$

Here, S is the standard deviation of n flux measurements $\langle \sigma_{err} \rangle$ the mean squared error and $\langle F_\gamma \rangle$ the average photon flux.

Chapter 6

Data Analysis

6.1 Swift Data

In this study, all public Swift X-ray data from Mrk 501, taken in 2015 and 2016 within a multiwavelength (MWL) monitoring campaign is analyzed. The full list of observation IDs can be found in Table 6.1. Of all 92 ObsIDs, 88 collected data in wt mode and only three data sets are in pc mode, the data from one observation (ObsID 00035023134) was empty. The ObsIDs were selected from the public *Swift* archive, searching for all observations of Mrk 501 during the years 2015 and 2016.

TABLE 6.1: ObsIDs of all *Swift*-XRT observations of Mrk 501 in 2015 and 2016.

Obsid	Mode	Date [MJD]	Exposure [s]	Total count rate [counts s ⁻¹]	Source count rate [counts s ⁻¹]
00035023150	wt	57684.200	1495.289	3.896 ± 0.053	3.808 ± 0.057
00035023148	wt	57678.144	1343.229	3.390 ± 0.053	3.324 ± 0.058
00035023149	wt	57681.335	1286.508	3.100 ± 0.052	3.035 ± 0.057
00035023143	wt	57606.911	1129.988	3.335 ± 0.058	3.282 ± 0.064
00035023126	wt	57525.101	1123.232	2.779 ± 0.054	2.703 ± 0.060
00092205018	wt	57248.417	94.696	4.858 ± 0.367	4.797 ± 0.491
00092205020	wt	57262.169	97.737	4.287 ± 0.350	4.267 ± 0.471
00035023144	wt	57608.916	1086.677	1.549 ± 0.044	1.468 ± 0.053
00035023109	wt	57473.067	1091.872	4.786 ± 0.069	4.704 ± 0.075
00035023133	wt	57566.042	1067.098	1.736 ± 0.046	1.645 ± 0.055
00092205021	wt	57269.088	44.605	3.408 ± 0.705	3.343 ± 0.987
00035023106	wt	57463.498	1063.002	6.500 ± 0.080	6.413 ± 0.086
00035023097	wt	57202.443	1040.853	5.244 ± 0.074	5.130 ± 0.080
00035023098	wt	57209.896	1048.899	4.013 ± 0.065	3.917 ± 0.072
00035023141	wt	57602.924	1043.707	3.246 ± 0.060	3.188 ± 0.067
00092398014	wt	57663.263	1031.779	3.397 ± 0.061	3.323 ± 0.068
00092205006	wt	57109.438	31.809	5.784 ± 0.995	5.634 ± 1.389
00092205005	wt	57105.452	749.025	6.426 ± 0.097	6.351 ± 0.105
00092398004	wt	57579.731	1041.315	2.862 ± 0.057	2.805 ± 0.064
00035023147	wt	57675.552	1023.207	4.016 ± 0.066	3.953 ± 0.073
00035023105	wt	57459.504	1042.498	6.040 ± 0.079	5.943 ± 0.084
00035023131	wt	57557.151	1015.394	3.708 ± 0.064	3.632 ± 0.071
00092398011	wt	57642.072	1012.392	4.022 ± 0.067	3.987 ± 0.073
00035023135	wt	57575.475	1030.313	3.745 ± 0.064	3.690 ± 0.071
00092205010	wt	57141.722	201.256	6.574 ± 0.218	6.440 ± 0.266
00035023124	wt	57518.321	1010.415	4.248 ± 0.068	4.195 ± 0.075
00092205001	wt	57080.828	166.089	5.527 ± 0.237	5.452 ± 0.301

Obsid	Mode	Date [MJD]	Exposure [s]	Total count rate [counts s ⁻¹]	Source count rate [counts s ⁻¹]
00035023118	wt	57496.066	989.602	4.966 ± 0.074	4.846 ± 0.080
00035023112	wt	57482.116	995.391	3.890 ± 0.066	3.822 ± 0.073
00035023142	wt	57604.932	1000.012	3.034 ± 0.060	2.995 ± 0.067
00092205012	wt	57206.035	95.764	5.315 ± 0.367	5.205 ± 0.488
00035023100	wt	57231.651	987.437	7.720 ± 0.090	7.622 ± 0.096
00092205015	wt	57227.458	25.428	5.388 ± 1.230	5.388 ± 1.728
00035023107	wt	57467.221	976.659	5.316 ± 0.077	5.250 ± 0.083
00035023122	wt	57514.090	991.412	4.685 ± 0.072	4.593 ± 0.079
00092205007	wt	57122.955	285.435	5.630 ± 0.164	5.529 ± 0.196
00035023137	wt	57591.906	970.071	4.542 ± 0.072	4.478 ± 0.079
00035023108	pc	57470.681	976.440	1.575 ± 0.046	1.476 ± 0.056
00035023125	wt	57522.442	959.043	3.995 ± 0.069	3.934 ± 0.076
00035023129	wt	57548.978	977.021	3.869 ± 0.067	3.831 ± 0.074
00035023103	wt	57455.450	982.282	6.287 ± 0.083	6.186 ± 0.088
00092205008	wt	57129.672	963.632	7.160 ± 0.088	7.011 ± 0.094
00092398001	wt	57498.456	957.847	4.698 ± 0.073	4.617 ± 0.080
00092398008	wt	57621.528	968.242	3.900 ± 0.068	3.823 ± 0.075
00035023116	wt	57492.473	969.633	3.478 ± 0.064	3.401 ± 0.072
00035023102	wt	57233.319	964.681	5.499 ± 0.079	5.399 ± 0.085
00092398005	wt	57586.263	966.393	3.939 ± 0.068	3.855 ± 0.075
00035023110	pc	57478.651	953.965	1.728 ± 0.047	1.642 ± 0.059
00035023094	wt	57174.722	973.004	6.487 ± 0.084	6.397 ± 0.090
00092398006	wt	57607.452	964.073	3.251 ± 0.063	3.215 ± 0.071
00092398007	wt	57614.224	958.921	0.070 ± 0.032	0.048 ± 0.046
00035023104	wt	57459.235	954.695	5.796 ± 0.081	5.705 ± 0.087
00035023092	wt	57139.453	967.295	5.721 ± 0.080	5.628 ± 0.086
00092205019	wt	57255.062	55.264	4.578 ± 0.586	4.561 ± 0.809
00092398010	wt	57635.556	949.940	2.960 ± 0.061	2.940 ± 0.069
00092205016	wt	57234.848	952.089	4.987 ± 0.076	4.915 ± 0.083
00092398013	wt	57656.763	949.104	2.730 ± 0.059	2.700 ± 0.068
00092205003	wt	57097.395	945.429	7.532 ± 0.091	7.443 ± 0.097
00092205017	wt	57241.689	4.110	5.839 ± 7.511	5.839 ± 10.620
00035023138	wt	57594.166	936.718	3.053 ± 0.062	2.961 ± 0.070
00035023128	wt	57544.984	936.684	2.491 ± 0.057	2.421 ± 0.066
00092398012	wt	57649.908	922.319	3.217 ± 0.064	3.187 ± 0.073
00035023099	wt	57230.194	925.136	5.058 ± 0.077	4.917 ± 0.084
00035023111	wt	57481.189	939.997	4.128 ± 0.070	4.047 ± 0.077
00092398009	wt	57628.241	934.079	3.251 ± 0.064	3.219 ± 0.072
00035023139	wt	57598.893	914.713	2.980 ± 0.062	2.912 ± 0.071
00035023145	wt	57610.897	918.912	3.258 ± 0.065	3.219 ± 0.073
00092205004	wt	57101.394	558.258	6.296 ± 0.113	6.176 ± 0.126
00035023113	wt	57484.432	903.557	2.444 ± 0.058	2.328 ± 0.067
00035023123	wt	57514.338	908.939	4.657 ± 0.075	4.566 ± 0.083
00035023130	wt	57553.082	899.344	4.192 ± 0.073	4.116 ± 0.080
00092205011	wt	57199.074	768.064	4.588 ± 0.082	4.484 ± 0.092
00035023114	wt	57488.164	894.170	5.501 ± 0.082	5.380 ± 0.089
00035023095	wt	57181.180	887.181	6.179 ± 0.087	6.083 ± 0.093
00035023140	wt	57600.931	888.387	1.337 ± 0.048	1.297 ± 0.059
00035023121	wt	57510.353	885.606	4.694 ± 0.077	4.632 ± 0.084

Obsid	Mode	Date [MJD]	Exposure [s]	Total count rate [counts s ⁻¹]	Source count rate [counts s ⁻¹]
00092205023	wt	57282.999	3.041	3.289 ± 10.147	3.289 ± 14.350
00035023101	wt	57232.720	871.778	5.492 ± 0.083	5.386 ± 0.090
00092205022	wt	57276.542	110.671	4.943 ± 0.323	4.943 ± 0.426
00035023119	pc	57500.065	806.626	1.920 ± 0.057	1.811 ± 0.069
00092398003	wt	57572.751	803.413	4.482 ± 0.079	4.423 ± 0.088
00092205002	wt	57087.899	91.492	5.509 ± 0.381	5.425 ± 0.509
00035023136	wt	57580.947	702.904	3.574 ± 0.079	3.490 ± 0.090
00035023096	wt	57188.165	674.185	4.760 ± 0.090	4.673 ± 0.101
00035023093	wt	57159.288	640.647	7.692 ± 0.114	7.538 ± 0.124
00092205014	wt	57220.817	17.971	1.558 ± 1.718	1.558 ± 2.429
00092205013	wt	57213.085	7.311	1.641 ± 4.220	1.641 ± 5.969
00092205009	wt	57136.406	315.969	7.210 ± 0.166	7.091 ± 0.193
00035023115	wt	57488.419	274.791	6.161 ± 0.173	6.060 ± 0.206
00035023127	wt	57540.944	230.723	3.012 ± 0.161	2.975 ± 0.209
00092398002	wt	57565.049	84.733	2.030 ± 0.374	1.917 ± 0.522
00035023134	-	57570.823	0.000	-nan ± -nan	0.000 ± 0.000

The used imaging mode is listed, as well as the exposure time, the count rate, the source count rate and the observation date in MJD. Where wt data was available, this data was used. For ObsID 00035023134 no data was available at all and it is therefore excluded from now on.

6.2 Data extraction

All data collected by *Swift* during 2015 and 2016 were first downloaded to, and then reprocessed on the University of Erlangen-Nürnberg's Astronomical Institute's servers, located at the Dr. Karl Remeis Observatory Bamberg. In order to later analyze the data, it had to be prepared and extracted first. This was done using Remeis extraction scripts, executing the HEASARC extraction pipeline. The extraction script takes the source's coordinates and places a circle with a radius of 20 arcseconds around it to define the source area. An annulus with an outer radius of 50 arcseconds and an inner radius of 35 arcseconds is then set around the source region, from which the background is extracted. The scripts then return the count rate for either observing mode, which enable us to check for pile-up. Due to the source's intense brightness in the X-ray band, all pc data had to be ignored as it was affected by significant pile-up, which is more thoroughly discussed in Sect. 6.3.

In order to find the intrinsic X-ray spectrum of a source, many factors have to be taken into account. First of all, information about the telescope and its efficiency is crucial. Therefore, an 'ancillary response function' (ARF) is required to describe the effective area of the detector, which is affected by both the instrument's architecture and potential inaccuracies such as technical defects or impurities of the detector's surface. These ARFs are kept up to date by the project's calibration team. Once all the telescope-specific influences are considered, the detector's properties need to be evaluated too, because the spectrum is not measured directly, but rather the number of counts per energy channel and time. In a perfect detector, each photon of a given energy results in a count in a particular spectral bin. As it happens, in real detectors not all photons with energy E will end up in the same bin because of noise or partial

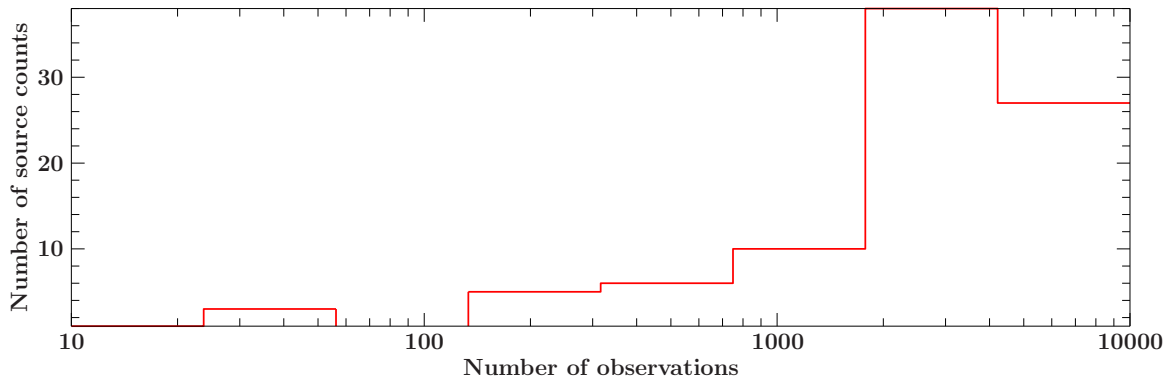


FIGURE 6.1: The number of observations over the respective source counts. 5 observations had less than 100 source counts total and are therefore ignored in the fitting process, as not enough bins with the required size are available to use χ^2 statistics.

absorption. Therefore, a Redistribution Matrix File (RMF) is created to account for this behavior.

6.3 Pile-up

For higher count rates, when working with CCDs an effect called pile-up is observed (Ballet, 1999). This means that, for instance, if two (or more) photons arrive at the detector in the same readout cycle, the detector will recognize them as a single photon with higher energy. As this is obviously a large error source, data has to be checked for pile-up before it can be used. To do so, the number of source counts in the whole energy range from 0.5 to 10 keV is divided by the exposure of the corresponding observation. In the *Swift*-XRT's wt mode, count rates $> 100 \text{ counts s}^{-1}$ are considered pile-up candidates (Romano et al., 2006), for pc observations, count rates larger than $0.5 \text{ counts s}^{-1}$ should be checked for pile-up (*UKSSDC | XRT threads*). The count rates of the respective observations are listed in Table 6.1. The three data sets taken in pc mode were excluded due to pile-up as the count rate was too large.

6.4 Background reduced data

The spectrum extracted from the source region is not free of counts that are actually background counts. These events are then subtracted from the source spectrum using Poisson statistics in order to have background reduced source counts. As χ^2 statistics require normally distributed data, sufficiently large numbers of events are needed to meet this requirement (see Sect. 5.2). Therefore, all data sets with less than 100 counts total are excluded from the analysis. Fig. 6.1 shows that five observations do not meet the criterion of 100 counts minimum and are thus ignored. Also, some observations did not have enough counts in either the 0.5 - 2 keV or the 2 - 10 keV band to produce two energy bins (see Sect. 6.5). These data are used in the fitting process but excluded from further computations due to their large errors. In the plots in Chapter 7, they are shown in gray.

6.5 Data processing

All processing of the data was carried out with the `ISIS` program. First, using the background reduced counts, the HR and the source count rate are computed as described in Sect. 5.1. To perform the model fit, a script was written in order to automatize the fitting process, as every data set requires the same steps. The spectra for each observation have to be binned first. Therefore, all counts below 0.5 keV and over 10 keV are ignored due to the detector's properties. Then, the bins are created so that each of them contains at least 30 counts, to be able to use χ^2 statistics (see Sect. 5.2). The spectrum is then fit using the *subplex* fit method and the *logpar* model combined with the *tbnew_simple* model introduced in Sect. 5.3. The minimal value of the column density n_H is set to $0.0142 \text{ } 10^{22} \text{ cm}^{-2}$, with this value taken from Kalberla et al. (2005). After evaluating the first model, the model fit function *cflux* is convolved with the best fit from the *logpar* model, again combined with the Galactic absorption model *tbnew_simple*, to compute the flux, with the normalization of the *logpar* frozen. Minimal and maximal energy in the flux model were fixed to 0.5 and 10 keV respectively. Fig. 6.2 shows an exemplary spectrum of the observation 00092205011, including residuals. The reduced χ^2 value is 1.0135, meaning the model neatly fits the spectrum. In order to quantify the flux variations in Mrk 501's spectrum over the two years, the fractional variability (see Sect. 5.4) is computed using the flux gained from the model *cflux*, taking into account its respective, symmetrized errors.

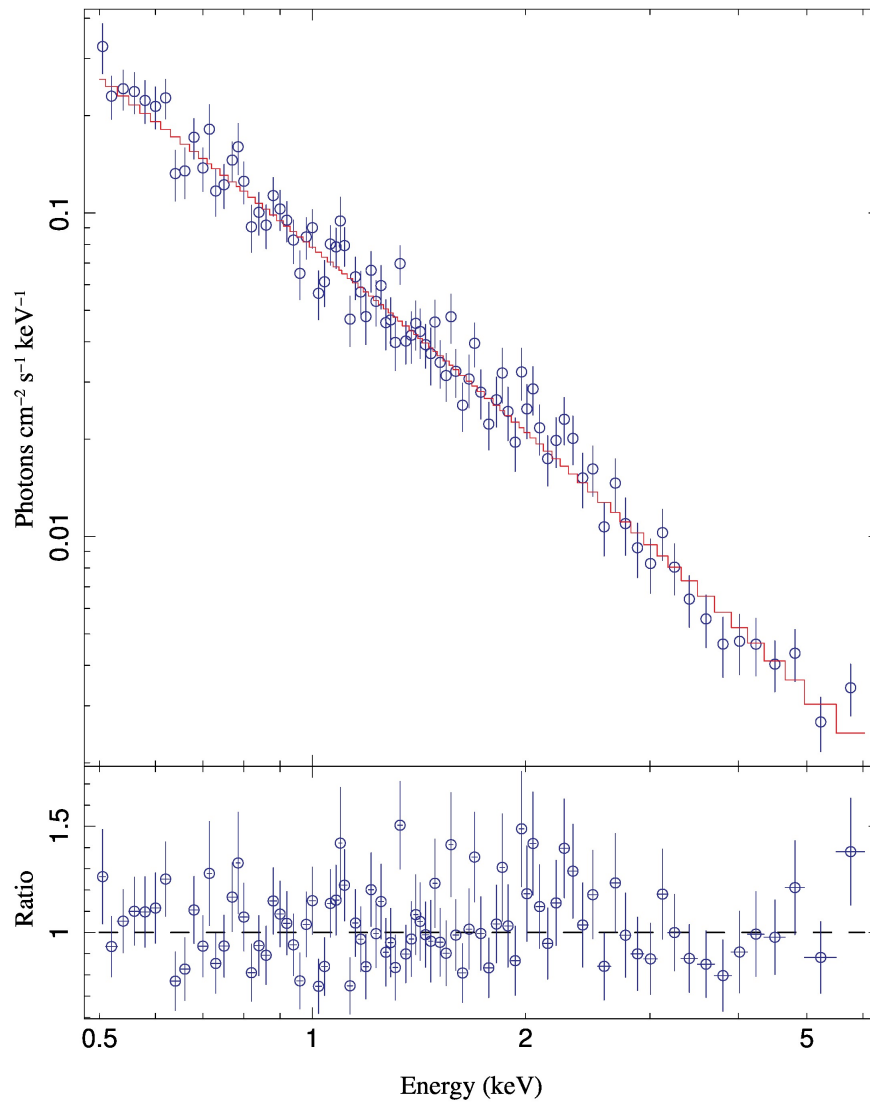


FIGURE 6.2: Exemplary spectrum of observation 00092205011 with residuals in the lower panel. The *logpar* model fits the data very well, $\chi^2_{red} = 1.0135$.

Chapter 7

Data evaluation

7.1 Phenomenological spectral Analysis

First, the information acquired with the counts script shall be presented, as it doesn't need a model or fit function. Therefore, Figs. 7.1 and 7.2 show the Hardness Ratio (HR) and the count rate over time in MJD, covering the years 2015 and 2016. A difference of 1 in MJD is equal to one day. Gray data points in plots indicate that these data did not have enough counts in either the 0.5-2 or the 2-10 keV band and are not used for the computation of mean values.

To compute the count rate, the number of source counts is divided by the observation's exposure time. It can be easily seen that both the count rate and the HR seem to be declining over the two year period.

7.2 Evaluation of the logpar model

In Fig. 7.3, the resulting reduced χ^2 values for each fit are shown. These values are scattered around 1, suggesting that the chosen function describes the data sufficiently well. In the appendix, Table A.1 shows all fit parameters with upper and lower limit for each observation, including a 'quality rating'. Perfectly fine data points are marked with a 100, piled-up pc data with 33, data excluded with the 100 counts photon cut are labeled 1 and data with too few counts in either band, still visible in the plot, are marked with 50 and plotted in gray. The quality ratings are used to distinguish the data points, their numerical values have been chosen arbitrarily. After all data has been fit using the mentioned model, the resulting parameters are

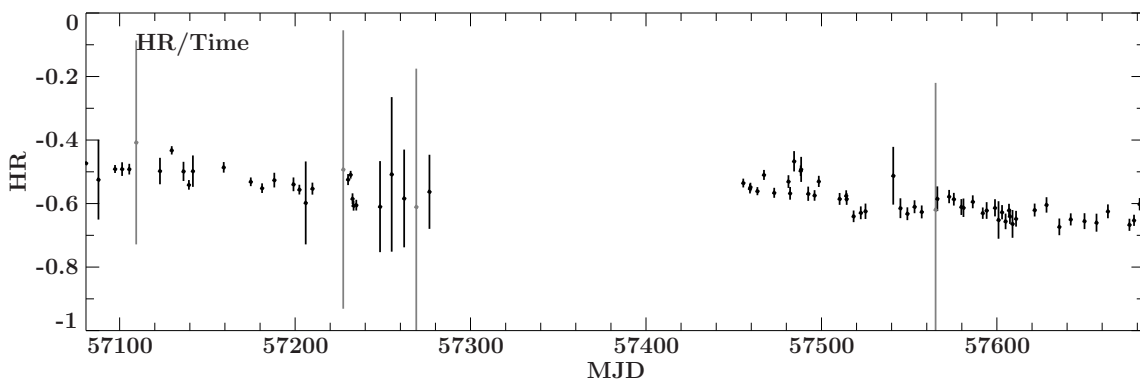


FIGURE 7.1: The Hardness Ratio HR over time in MJD. A weak declining trend can be seen, indicating a softening of the spectrum over time.

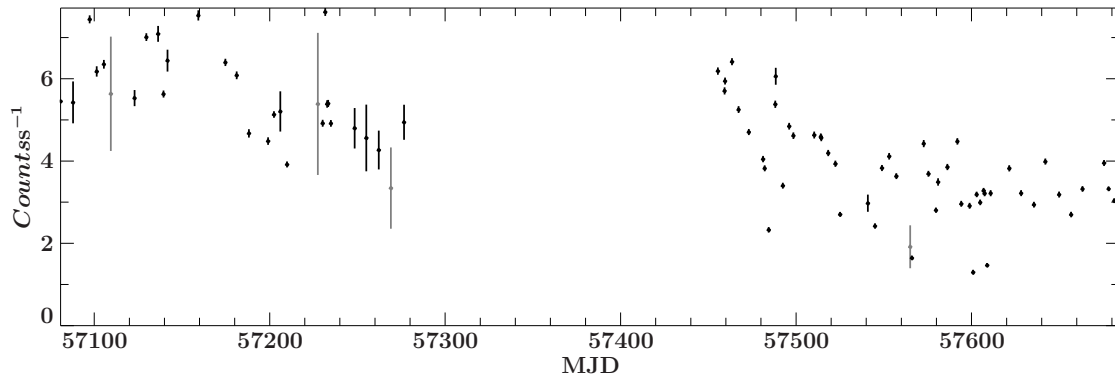


FIGURE 7.2: The count rate over time in MJD. The count rate seems to decrease as a function of time.

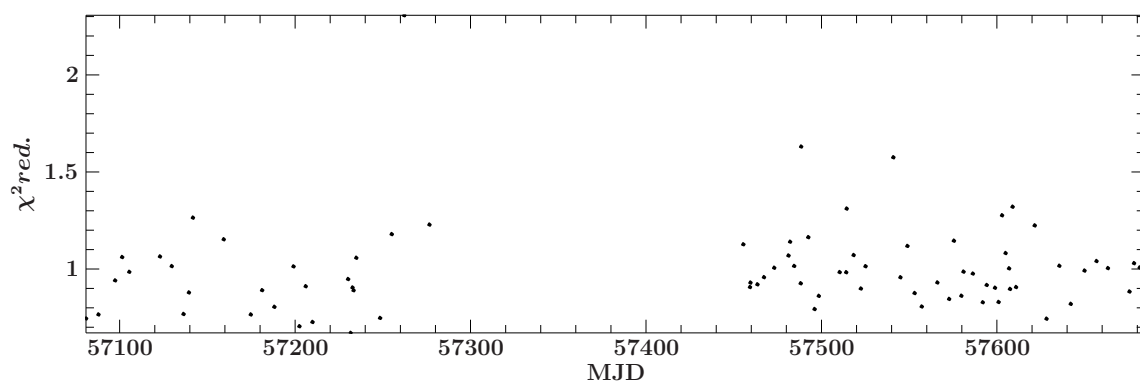


FIGURE 7.3: The χ^2_{red} values for each observation, plotted over the time axis. The values scatter around the optimal reduced χ^2 of 1.

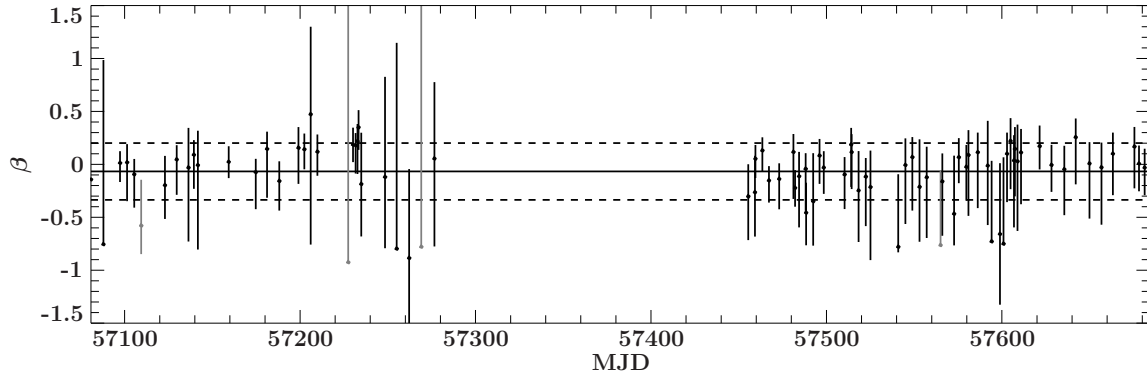


FIGURE 7.4: The curvature parameter β of the *logpar* model over time. Mean value and one standard deviation to both sides are plotted to illustrate the constancy of β .

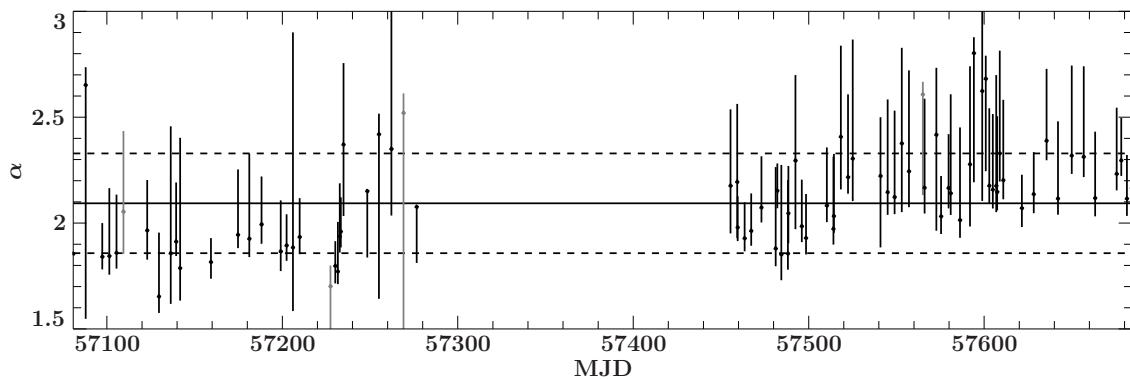


FIGURE 7.5: The photon index α from the *logpar* model plotted over time. Mean value and standard deviation are included to better visualize the trend of a rising α as a function of time.

plotted over time or against each other respectively. Fig. 7.4 shows the time dependence of the curvature parameter β .

This parameter does not change significantly over the two year period and has a mean value of -0.07 ± 0.27 . This means that the computed α values are directly related to the photon index as the spectrum is not significantly curved at the pivot energy of 1 keV. Fig. 7.5 shows the photon index plotted over time.

The data seems to be more or less equally distributed around the mean value of 2.09 ± 0.24 , but after the observation break, a rise in α can be seen. In Fig. 7.6 the flux is plotted over time. A decline is visible, especially after the observation break. To better illustrate this, the mean value is shown. No definite flaring activity can be seen, but some variability is exhibited. The computation of the fractional variability yields a value of $F_{var} = 0.370 \pm 0.018$.

Fig. 7.7 shows the photon index plotted over the flux. Higher fluxes seem to correspond to lower photon indices and vice versa. The result of linear regression is shown to illustrate this behavior.

7.3 Discussion

The 2015 to 2016 data from Mrk 501, compared with data from other observations, e.g. Albert et al. (2007) or Chakraborty et al. (2015), indicates that the source is in

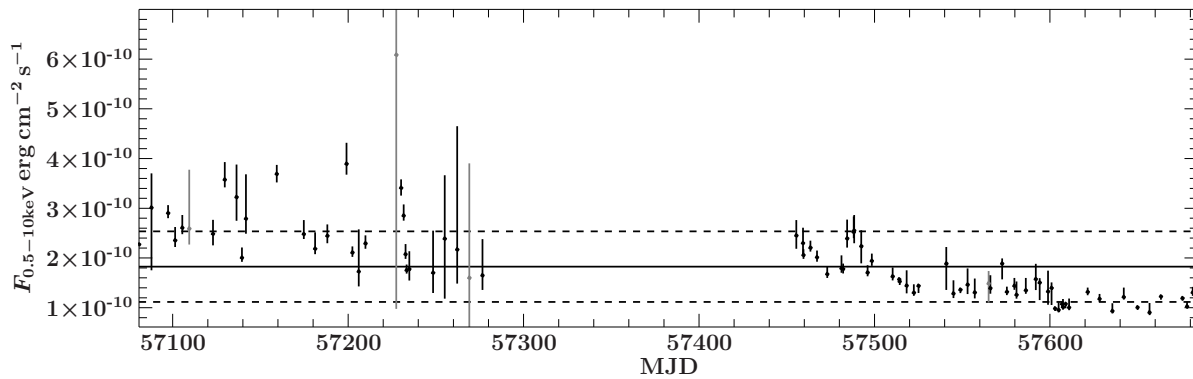


FIGURE 7.6: The flux computed with the model *cflux* over time. Mean value and standard deviation underline the declining of the flux during the two years.

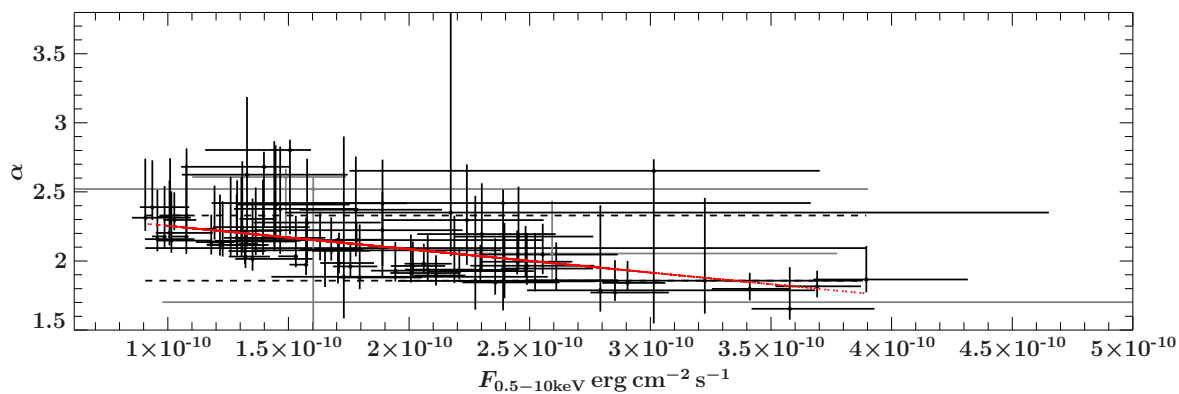


FIGURE 7.7: Photon index α plotted over the flux. Higher fluxes seem to show lower photon indices and vice versa. This is a strong indication of the *harder when brighter* trend. A linear regression line is drawn to better illustrate this behavior.

a decreasing quiescent state during these two years. No obvious short time variability can be seen, and no periodical long time variability either, even though the fractional variability F_{var} was found to be at 0.370 ± 0.018 , which is a regular value for this object in the X-ray band (e.g. Aleksić et al. (2015), Ahnen et al. (2016)), indicating moderate variability. The fact, that the *logpar* model described the data so well confirms that the X-ray spectrum of Mrk 501 is of nonthermal origin and does not show features like emission lines. This means the emission can definitely be attributed to a relativistic jet. As can be seen in Fig. 7.4, the curvature is around zero, indicating that the synchrotron peak lies at energies lower than 0.5 keV, making the spectrum also consistent with a powerlaw fit. The phenomenological data shown in Figs. 7.1 and 7.2 seem to indicate a trend of the brightness decreasing and the spectrum simultaneously softening. This looks like the well known *harder when brighter* trend in blazars, the cause of which has not yet been understood, but from this variation alone, it is not possible to differ between an intrinsic spectral change or absorption effects. A better indicator for the cause of this behavior is the modelled data, as an absorption model is used. The evolution of the photon index over time, shown in Fig. 7.5, indicates the same trend as the HR over time: a spectral softening over the observed period. At the same time, the temporal evolution of the flux shows the same behavior as the count rate (see Figs. 7.6 and 7.2), namely a decline in brightness. Therefore, the observed trend of a softening and dimming spectrum has to be an intrinsic one, due to changes in the emission region, like a shifting of the synchrotron emission to lower energies when the source becomes fainter. This dependency is seen even more clearly in Fig. 7.7, where α is plotted against the flux. The correlation between larger fluxes and lower photon indices and therefore softer spectra can clearly be accounted to the *harder when brighter* trend, apparently also showing in low flux states and not only during flaring activity.

7.4 Conclusion

The spectral analysis of two years of *Swift*-XRT data of the blazar Mrk 501 has shown that the source was in a quiescent state with declining brightness in 2015 and 2016, showing regular flux variability. Also, the known *harder when brighter* trend has been observed even during a low flux state, indicating changes in the emission region that depend on the AGN's brightness. The proclaimed target of the Würzburg blazar study is to observe a blazar during a flare. In order to do so, first, the definition of a flare has to be settled. This can not be done without profound knowledge on the spectral properties in a quiescent, or non-flaring state. Also, after a hypothetical flare has been observed, to quantify the spectral changes, a baseline is needed to compare the data taken during a flare to. As Mrk 501 has been in a quiescent state over the years of 2015 and 2016, this study gives a good starting point for further X-ray analysis of Mrk 501, ideally during flaring states, by offering a long-time observation of the source during a declining quiescent state, thereby providing the needed baseline.

Appendix A

Appendix

The following table A.1 includes all best-fit parameters with errors for each observation. It is continued over the next pages.

TABLE A.1: All best-fit parameter values and errors for the convolution of *logpar* with *cflux*.

Obsid	n_H [10^{22} cm^{-2}]	α	β	$F_{0.5-10}$ [$10^{-10} \text{ erg cm}^{-2} \text{ s}^{-1}$]	χ^2/DOF	HR	quality
00035023150	$0.014^{+0.068}_{-0.000}$	$2.167^{+0.314}_{-0.065}$	$-0.026^{+0.144}_{-0.381}$	$1.286^{+0.171}_{-0.054}$	1.18	-0.62 ± 0.01	100
00035023148	$0.014^{+0.042}_{-0.000}$	$2.296^{+0.200}_{-0.074}$	$0.008^{+0.170}_{-0.263}$	$1.027^{+0.091}_{-0.045}$	1.03	-0.65 ± 0.02	100
00035023149	$0.014^{+0.044}_{-0.000}$	$2.116^{+0.206}_{-0.082}$	$-0.030^{+0.177}_{-0.262}$	$1.306^{+0.112}_{-0.066}$	1.01	-0.60 ± 0.02	100
00035023143	$0.024^{+0.113}_{-0.010}$	$2.177^{+0.522}_{-0.125}$	$0.038^{+0.238}_{-0.633}$	$1.077^{+0.000}_{-0.076}$	1.00	-0.62 ± 0.02	100
00035023126	$0.038^{+0.122}_{-0.024}$	$2.305^{+0.562}_{-0.201}$	$-0.213^{+0.344}_{-0.691}$	$1.442^{+0.000}_{-0.144}$	1.01	-0.62 ± 0.02	100
00092205018	$0.014^{+0.188}_{-0.000}$	$2.151^{+0.000}_{-0.314}$	$-0.118^{+0.945}_{-0.675}$	$1.705^{+0.846}_{-0.410}$	0.75	-0.61 ± 0.14	100
00092205020	$0.014^{+0.239}_{-0.000}$	$2.350^{+1.448}_{-0.315}$	$-0.884^{+0.840}_{-1.860}$	$2.172^{+2.479}_{-0.686}$	2.31	-0.58 ± 0.15	100
00035023144	$0.014^{+0.102}_{-0.000}$	$2.330^{+0.485}_{-0.133}$	$0.029^{+0.346}_{-0.658}$	$1.078^{+0.000}_{-0.089}$	1.32	-0.66 ± 0.04	100
00035023109	$0.014^{+0.053}_{-0.000}$	$2.074^{+0.242}_{-0.071}$	$-0.136^{+0.146}_{-0.288}$	$1.677^{+0.160}_{-0.078}$	1.01	-0.57 ± 0.02	100
00035023133	$0.014^{+0.090}_{-0.000}$	$2.167^{+0.420}_{-0.122}$	$-0.160^{+0.263}_{-0.515}$	$1.395^{+0.259}_{-0.112}$	0.93	-0.58 ± 0.04	100
00092205021	$0.014^{+0.591}_{-0.000}$	$2.521^{+0.092}_{-1.114}$	$-0.778^{+4.778}_{-0.003}$	$1.603^{+2.300}_{-0.990}$	-1.33	-0.61 ± 0.44	50
00035023106	$0.014^{+0.037}_{-0.000}$	$1.928^{+0.170}_{-0.062}$	$0.132^{+0.124}_{-0.205}$	$2.208^{+0.140}_{-0.079}$	0.92	-0.56 ± 0.01	100
00035023097	$0.014^{+0.031}_{-0.000}$	$1.895^{+0.147}_{-0.073}$	$0.143^{+0.147}_{-0.190}$	$2.112^{+0.122}_{-0.091}$	0.71	-0.56 ± 0.02	100
00035023098	$0.014^{+0.039}_{-0.000}$	$1.935^{+0.183}_{-0.081}$	$0.120^{+0.162}_{-0.229}$	$2.295^{+0.160}_{-0.109}$	0.73	-0.55 ± 0.02	100
00035023141	$0.014^{+0.078}_{-0.000}$	$2.177^{+0.365}_{-0.085}$	$0.101^{+0.199}_{-0.458}$	$0.987^{+0.000}_{-0.051}$	1.28	-0.63 ± 0.02	100
00092398014	$0.014^{+0.067}_{-0.000}$	$2.119^{+0.313}_{-0.087}$	$0.101^{+0.199}_{-0.393}$	$1.228^{+0.000}_{-0.066}$	1.00	-0.62 ± 0.02	100
00092205006	$0.014^{+0.061}_{-0.000}$	$2.054^{+0.381}_{-0.200}$	$-0.577^{+0.431}_{-0.271}$	$2.593^{+1.182}_{-0.323}$	INF	-0.41 ± 0.32	50
00092205005	$0.014^{+0.061}_{-0.000}$	$1.860^{+0.274}_{-0.075}$	$-0.093^{+0.144}_{-0.316}$	$2.610^{+0.255}_{-0.131}$	0.99	-0.49 ± 0.02	100

Obsid	n_H [10^{22} cm^{-2}]	α	β	$F_{0.5-10}$ [$10^{-10} \text{ erg cm}^{-2} \text{ s}^{-1}$]	χ^2/DOF	HR	quality
00092398004	$0.014^{+0.054}_{-0.000}$	$2.166^{+0.254}_{-0.096}$	$-0.023^{+0.206}_{-0.320}$	$1.442^{+0.157}_{-0.082}$	0.86	-0.61 ± 0.02	100
00035023147	$0.014^{+0.067}_{-0.000}$	$2.233^{+0.312}_{-0.078}$	$0.169^{+0.185}_{-0.395}$	$1.194^{+0.000}_{-0.053}$	0.88	-0.67 ± 0.02	100
00035023105	$0.014^{+0.031}_{-0.000}$	$1.980^{+0.146}_{-0.065}$	$0.055^{+0.129}_{-0.183}$	$2.061^{+0.115}_{-0.080}$	0.93	-0.55 ± 0.01	100
00035023131	$0.034^{+0.104}_{-0.020}$	$2.245^{+0.476}_{-0.170}$	$-0.121^{+0.288}_{-0.575}$	$1.309^{+0.279}_{-0.121}$	0.81	-0.63 ± 0.02	100
00092398011	$0.014^{+0.079}_{-0.000}$	$2.116^{+0.365}_{-0.077}$	$0.257^{+0.176}_{-0.446}$	$1.216^{+0.189}_{-0.054}$	0.82	-0.65 ± 0.02	100
00035023135	$0.014^{+0.040}_{-0.000}$	$2.032^{+0.190}_{-0.084}$	$0.068^{+0.179}_{-0.246}$	$1.322^{+0.102}_{-0.069}$	1.15	-0.59 ± 0.02	100
00092205010	$0.014^{+0.160}_{-0.000}$	$1.788^{+0.615}_{-0.154}$	$-0.006^{+0.325}_{-0.798}$	$2.793^{+0.890}_{-0.303}$	1.26	-0.50 ± 0.05	100
00035023124	$0.054^{+0.095}_{-0.039}$	$2.408^{+0.430}_{-0.249}$	$-0.246^{+0.371}_{-0.488}$	$1.447^{+0.306}_{-0.159}$	1.07	-0.64 ± 0.02	100
00092205001	$0.014^{+0.151}_{-0.000}$	$1.856^{+0.615}_{-0.208}$	$-0.142^{+0.436}_{-0.679}$	$2.275^{+0.594}_{-0.320}$	0.75	-0.47 ± 0.07	100
00035023118	$0.014^{+0.048}_{-0.000}$	$1.985^{+0.219}_{-0.075}$	$0.084^{+0.156}_{-0.269}$	$1.709^{+0.146}_{-0.078}$	0.79	-0.57 ± 0.02	100
00035023112	$0.014^{+0.025}_{-0.000}$	$2.153^{+0.128}_{-0.084}$	$-0.221^{+0.167}_{-0.179}$	$1.782^{+0.105}_{-0.093}$	1.14	-0.57 ± 0.02	100
00035023142	$0.014^{+0.076}_{-0.000}$	$2.158^{+0.357}_{-0.089}$	$0.222^{+0.215}_{-0.457}$	$0.957^{+0.154}_{-0.052}$	1.08	-0.66 ± 0.02	100
00092205012	$0.014^{+0.240}_{-0.000}$	$1.885^{+1.015}_{-0.301}$	$0.474^{+0.826}_{-1.232}$	$1.730^{+0.845}_{-0.301}$	0.91	-0.60 ± 0.13	100
00035023100	$0.014^{+0.053}_{-0.000}$	$1.772^{+0.234}_{-0.060}$	$0.180^{+0.116}_{-0.266}$	$2.853^{+0.223}_{-0.101}$	0.67	-0.51 ± 0.01	100
00092205015	$0.014^{+0.520}_{-0.000}$	$1.702^{+0.098}_{-0.786}$	$-0.924^{+4.360}_{-0.003}$	$6.088^{+8.546}_{-5.110}$	-0.12	-0.49 ± 0.44	50
00035023107	$0.014^{+0.038}_{-0.000}$	$1.964^{+0.176}_{-0.071}$	$-0.151^{+0.134}_{-0.210}$	$2.016^{+0.134}_{-0.091}$	0.96	-0.51 ± 0.02	100
00035023122	$0.014^{+0.075}_{-0.000}$	$1.973^{+0.341}_{-0.075}$	$0.189^{+0.155}_{-0.402}$	$1.573^{+0.000}_{-0.069}$	0.98	-0.58 ± 0.02	100
00092205007	$0.014^{+0.049}_{-0.000}$	$1.966^{+0.238}_{-0.139}$	$-0.196^{+0.276}_{-0.319}$	$2.488^{+0.280}_{-0.234}$	1.06	-0.50 ± 0.04	100
00035023137	$0.065^{+0.101}_{-0.051}$	$2.278^{+0.463}_{-0.294}$	$-0.011^{+0.422}_{-0.563}$	$1.577^{+0.305}_{-0.222}$	0.83	-0.63 ± 0.02	100
00035023108	$0.014^{+0.056}_{-0.000}$	$1.716^{+0.000}_{-0.000}$	$-0.071^{+0.000}_{-0.000}$	$0.956^{+0.000}_{-0.000}$	0.90	-0.49 ± 0.05	33
00035023125	$0.014^{+0.084}_{-0.000}$	$2.218^{+0.390}_{-0.079}$	$-0.115^{+0.174}_{-0.469}$	$1.305^{+0.167}_{-0.066}$	0.90	-0.63 ± 0.02	100
00035023129	$0.014^{+0.089}_{-0.000}$	$2.123^{+0.408}_{-0.081}$	$0.069^{+0.188}_{-0.506}$	$1.365^{+0.000}_{-0.072}$	1.12	-0.63 ± 0.02	100
00035023103	$0.052^{+0.080}_{-0.038}$	$2.177^{+0.361}_{-0.225}$	$-0.302^{+0.303}_{-0.414}$	$2.454^{+0.310}_{-0.267}$	1.13	-0.54 ± 0.01	100
00092205008	$0.017^{+0.070}_{-0.003}$	$1.654^{+0.301}_{-0.078}$	$0.047^{+0.135}_{-0.334}$	$3.578^{+0.352}_{-0.158}$	1.01	-0.43 ± 0.01	100
00092398001	$0.014^{+0.045}_{-0.000}$	$1.930^{+0.207}_{-0.078}$	$-0.029^{+0.154}_{-0.250}$	$1.943^{+0.147}_{-0.100}$	0.86	-0.53 ± 0.02	100
00092398008	$0.014^{+0.032}_{-0.000}$	$2.071^{+0.157}_{-0.090}$	$0.173^{+0.194}_{-0.221}$	$1.319^{+0.084}_{-0.068}$	1.22	-0.62 ± 0.02	100
00035023116	$0.071^{+0.096}_{-0.057}$	$2.296^{+0.403}_{-0.324}$	$-0.348^{+0.453}_{-0.420}$	$2.239^{+0.319}_{-0.348}$	1.16	-0.57 ± 0.02	100
00035023102	$0.014^{+0.034}_{-0.000}$	$1.960^{+0.161}_{-0.075}$	$0.351^{+0.161}_{-0.214}$	$1.757^{+0.112}_{-0.072}$	0.89	-0.61 ± 0.02	100
00092398005	$0.014^{+0.096}_{-0.000}$	$2.015^{+0.437}_{-0.084}$	$0.116^{+0.185}_{-0.529}$	$1.351^{+0.249}_{-0.071}$	0.98	-0.59 ± 0.02	100

Obsid	n_H [10^{22} cm^{-2}]	α	β	$F_{0.5-10}$ [$10^{-10} \text{ erg cm}^{-2} \text{ s}^{-1}$]	χ^2/DOF	HR	quality
00035023110	$0.014^{+0.075}_{-0.000}$	$1.574^{+0.000}_{-0.000}$	$0.131^{+0.000}_{-0.000}$	$0.832^{+0.000}_{-0.000}$	0.88	-0.43 ± 0.04	33
00035023094	$0.014^{+0.069}_{-0.000}$	$1.945^{+0.308}_{-0.064}$	$-0.073^{+0.125}_{-0.350}$	$2.483^{+0.280}_{-0.102}$	0.77	-0.53 ± 0.01	100
00092398006	$0.014^{+0.076}_{-0.000}$	$2.148^{+0.356}_{-0.088}$	$0.148^{+0.204}_{-0.450}$	$1.015^{+0.160}_{-0.055}$	0.90	-0.64 ± 0.02	100
00092398007	$0.014^{+0.142}_{-0.000}$	$2.466^{+0.094}_{-0.376}$	$-0.788^{+0.556}_{-0.003}$	$1.367^{+0.925}_{-0.268}$	-0.00	-0.69 ± 1.48	1
00035023104	$0.063^{+0.081}_{-0.048}$	$2.195^{+0.368}_{-0.266}$	$-0.263^{+0.344}_{-0.420}$	$2.301^{+0.307}_{-0.268}$	0.91	-0.55 ± 0.02	100
00035023092	$0.014^{+0.062}_{-0.000}$	$1.913^{+0.278}_{-0.069}$	$0.092^{+0.138}_{-0.323}$	$2.007^{+0.204}_{-0.085}$	0.88	-0.54 ± 0.02	100
00092205019	$0.116^{+0.179}_{-0.101}$	$2.420^{+0.097}_{-0.778}$	$-0.796^{+1.944}_{-0.003}$	$2.390^{+1.275}_{-1.208}$	1.18	-0.51 ± 0.24	100
00092398010	$0.014^{+0.071}_{-0.000}$	$2.389^{+0.339}_{-0.093}$	$-0.045^{+0.220}_{-0.434}$	$0.936^{+0.153}_{-0.052}$	1.02	-0.67 ± 0.03	100
00092205016	$0.088^{+0.092}_{-0.074}$	$2.371^{+0.384}_{-0.338}$	$-0.185^{+0.484}_{-0.497}$	$1.779^{+0.357}_{-0.233}$	1.06	-0.61 ± 0.02	100
00092398013	$0.014^{+0.091}_{-0.000}$	$2.313^{+0.427}_{-0.096}$	$-0.027^{+0.233}_{-0.543}$	$0.907^{+0.188}_{-0.055}$	1.04	-0.66 ± 0.03	100
00092205003	$0.014^{+0.035}_{-0.000}$	$1.842^{+0.159}_{-0.061}$	$0.014^{+0.110}_{-0.181}$	$2.906^{+0.157}_{-0.105}$	0.94	-0.49 ± 0.01	100
00092205017	$0.072^{+0.200}_{-0.058}$	$2.011^{+0.062}_{-1.005}$	$-0.869^{+1.592}_{-0.003}$	$5.928^{+2.905}_{-3.558}$	0.93	-0.33 ± 2.28	1
00035023138	$0.172^{+0.037}_{-0.133}$	$2.803^{+0.075}_{-0.610}$	$-0.727^{+0.761}_{-0.003}$	$1.506^{+0.087}_{-0.352}$	0.92	-0.62 ± 0.03	100
00035023128	$0.014^{+0.094}_{-0.000}$	$2.146^{+0.438}_{-0.108}$	$-0.006^{+0.251}_{-0.558}$	$1.287^{+0.264}_{-0.092}$	0.96	-0.61 ± 0.03	100
00092398012	$0.014^{+0.091}_{-0.000}$	$2.319^{+0.425}_{-0.087}$	$0.009^{+0.201}_{-0.522}$	$1.009^{+0.000}_{-0.053}$	0.99	-0.66 ± 0.02	100
00035023099	$0.014^{+0.023}_{-0.000}$	$1.798^{+0.116}_{-0.084}$	$0.187^{+0.160}_{-0.165}$	$3.412^{+0.170}_{-0.157}$	0.95	-0.52 ± 0.02	100
00035023111	$0.014^{+0.085}_{-0.000}$	$1.880^{+0.384}_{-0.084}$	$0.118^{+0.169}_{-0.444}$	$1.795^{+0.258}_{-0.092}$	1.07	-0.53 ± 0.02	100
00092398009	$0.014^{+0.041}_{-0.000}$	$2.137^{+0.198}_{-0.090}$	$-0.005^{+0.189}_{-0.256}$	$1.180^{+0.097}_{-0.064}$	0.74	-0.60 ± 0.02	100
00035023139	$0.118^{+0.124}_{-0.104}$	$2.624^{+0.562}_{-0.520}$	$-0.657^{+0.668}_{-0.669}$	$1.328^{+0.417}_{-0.270}$	0.90	-0.61 ± 0.03	100
00035023145	$0.014^{+0.081}_{-0.000}$	$2.203^{+0.379}_{-0.091}$	$0.114^{+0.221}_{-0.490}$	$1.007^{+0.179}_{-0.057}$	0.91	-0.65 ± 0.02	100
00092205004	$0.014^{+0.071}_{-0.000}$	$1.845^{+0.320}_{-0.089}$	$0.020^{+0.171}_{-0.368}$	$2.357^{+0.267}_{-0.135}$	1.06	-0.49 ± 0.02	100
00035023113	$0.014^{+0.094}_{-0.000}$	$1.853^{+0.422}_{-0.123}$	$-0.111^{+0.229}_{-0.484}$	$2.395^{+0.378}_{-0.186}$	1.02	-0.47 ± 0.03	100
00035023123	$0.014^{+0.064}_{-0.000}$	$2.033^{+0.293}_{-0.080}$	$0.117^{+0.168}_{-0.351}$	$1.531^{+0.000}_{-0.073}$	1.31	-0.59 ± 0.02	100
00035023130	$0.072^{+0.100}_{-0.057}$	$2.377^{+0.451}_{-0.325}$	$-0.211^{+0.448}_{-0.520}$	$1.466^{+0.323}_{-0.191}$	0.88	-0.61 ± 0.02	100
00092205011	$0.014^{+0.060}_{-0.000}$	$1.866^{+0.241}_{-0.093}$	$0.157^{+0.195}_{-0.342}$	$3.895^{+0.421}_{-0.219}$	1.01	-0.54 ± 0.02	100
00035023114	$0.014^{+0.078}_{-0.000}$	$1.856^{+0.347}_{-0.077}$	$-0.042^{+0.147}_{-0.396}$	$2.522^{+0.315}_{-0.123}$	0.93	-0.50 ± 0.02	100
00035023095	$0.018^{+0.089}_{-0.004}$	$1.927^{+0.401}_{-0.087}$	$0.147^{+0.162}_{-0.463}$	$2.188^{+0.329}_{-0.111}$	0.89	-0.55 ± 0.02	100
00035023140	$0.091^{+0.063}_{-0.077}$	$2.682^{+0.109}_{-0.437}$	$-0.749^{+0.816}_{-0.003}$	$1.399^{+0.110}_{-0.343}$	0.83	-0.65 ± 0.06	100
00035023121	$0.014^{+0.059}_{-0.000}$	$2.083^{+0.274}_{-0.079}$	$-0.095^{+0.163}_{-0.328}$	$1.631^{+0.179}_{-0.083}$	0.98	-0.59 ± 0.02	100

Obsid	n_H [10^{22} cm^{-2}]	α	β	$F_{0.5-10}$ [$10^{-10} \text{ erg cm}^{-2} \text{ s}^{-1}$]	χ^2/DOF	HR	quality
00092205023	$0.515^{+1.082}_{-0.501}$	$2.384^{+1.616}_{-2.384}$	$3.976^{+0.024}_{-4.490}$	$1.737^{+29.797}_{-1.038}$	1.24	-1.00 ± 8.01	1
00035023101	$0.014^{+0.054}_{-0.000}$	$1.937^{+0.251}_{-0.076}$	$0.218^{+0.163}_{-0.310}$	$2.077^{+0.203}_{-0.094}$	0.90	-0.58 ± 0.02	100
00092205022	$0.014^{+0.178}_{-0.000}$	$2.077^{+0.000}_{-0.265}$	$0.055^{+0.721}_{-0.831}$	$1.651^{+0.729}_{-0.295}$	1.23	-0.56 ± 0.12	100
00035023119	$0.014^{+0.151}_{-0.000}$	$1.776^{+0.000}_{-0.000}$	$0.001^{+0.000}_{-0.000}$	$0.983^{+0.000}_{-0.000}$	0.87	-0.51 ± 0.05	33
00092398003	$0.110^{+0.081}_{-0.096}$	$2.417^{+0.316}_{-0.454}$	$-0.466^{+0.548}_{-0.300}$	$1.890^{+0.103}_{-0.319}$	0.85	-0.58 ± 0.02	100
00092205002	$0.315^{+0.159}_{-0.301}$	$2.652^{+0.084}_{-1.104}$	$-0.754^{+1.740}_{-0.003}$	$3.014^{+0.688}_{-1.262}$	0.77	-0.52 ± 0.13	100
00035023136	$0.014^{+0.101}_{-0.000}$	$2.141^{+0.467}_{-0.103}$	$0.089^{+0.233}_{-0.576}$	$1.261^{+0.267}_{-0.078}$	0.99	-0.61 ± 0.03	100
00035023096	$0.014^{+0.048}_{-0.000}$	$1.994^{+0.226}_{-0.092}$	$-0.156^{+0.185}_{-0.281}$	$2.448^{+0.228}_{-0.151}$	0.81	-0.53 ± 0.02	100
00035023093	$0.014^{+0.022}_{-0.000}$	$1.816^{+0.113}_{-0.079}$	$0.025^{+0.146}_{-0.155}$	$3.691^{+0.182}_{-0.173}$	1.15	-0.49 ± 0.02	100
00092205014	$0.014^{+0.104}_{-0.000}$	$2.288^{+0.061}_{-0.489}$	$-0.819^{+1.046}_{-0.003}$	$1.737^{+0.953}_{-0.691}$	1.56	-0.64 ± 2.36	1
00092205013	$0.014^{+0.225}_{-0.000}$	$2.324^{+0.520}_{-0.833}$	$-0.709^{+2.016}_{-0.106}$	$1.980^{+3.093}_{-0.711}$	1.12	-0.33 ± 4.55	1
00092205009	$0.042^{+0.137}_{-0.028}$	$1.857^{+0.600}_{-0.239}$	$-0.030^{+0.374}_{-0.699}$	$3.226^{+0.655}_{-0.476}$	0.77	-0.50 ± 0.03	100
00035023115	$0.014^{+0.045}_{-0.000}$	$2.047^{+0.223}_{-0.142}$	$-0.455^{+0.281}_{-0.309}$	$2.554^{+0.311}_{-0.256}$	1.63	-0.49 ± 0.04	100
00035023127	$0.046^{+0.081}_{-0.032}$	$2.223^{+0.277}_{-0.338}$	$-0.778^{+0.685}_{-0.053}$	$1.889^{+0.333}_{-0.531}$	1.58	-0.51 ± 0.09	100
00092398002	$0.052^{+0.104}_{-0.038}$	$2.608^{+0.059}_{-0.476}$	$-0.762^{+0.700}_{-0.003}$	$1.489^{+0.250}_{-0.388}$	INF	-0.62 ± 0.40	50

The column ‘quality’ shows the quality index (see Sect. 7.2) of the measurement. 100 means there was nothing wrong with the data, 50 means it was fitted but excluded from mean-calculation because the individual bands (soft: 0.5 - 2 keV and hard: 2 - 10 keV) didn’t have enough counts for at least 2 bins. 33 means it was taken in pc mode and excluded due to pile-up and 1 means it was excluded directly because of less than 100 counts total.

Bibliography

- Abdo, A. A. et al. (2010). "The Spectral Energy Distribution of Fermi Bright Blazars". In: *The Astrophysical Journal* 716, pp. 30–70.
- Acciari, V. A. et al. (2011). "Spectral Energy Distribution of Markarian 501: Quiescent State Versus Extreme Outburst". In: *The Astrophysical Journal* 729.1, p. 2.
- Ahnen, M. L. et al. (2016). "Multiband variability studies and novel broadband SED modeling of Mrk 501 in 2009". In: *arXiv:1612.09472 [astro-ph]*.
- Albert, J. et al. (2007). "Variable Very High Energy γ -Ray Emission from Markarian 501". In: *The Astrophysical Journal* 669.2, p. 862.
- Aleksić, J. et al. (2015). "Multiwavelength observations of Mrk 501 in 2008". In: *Astronomy & Astrophysics* 573, A50.
- Antonucci, Robert (1993). "Unified models for active galactic nuclei and quasars". In: *Annual Review of Astronomy and Astrophysics* 31, pp. 473–521.
- Ballet, J. (1999). "Pile-up on X-ray CCD instruments". In: *Astronomy and Astrophysics Supplement Series* 135, pp. 371–381.
- Barthelmy, Scott D. et al. (2005). "The Burst Alert Telescope (BAT) on the SWIFT Midex Mission". In: *Space Science Reviews* 120, pp. 143–164.
- Bloom, Steven D. et al. (1993). "Examining the synchrotron self-Compton model for blazars". In: *AIP Conference Proceedings* 280.1, pp. 578–582.
- Burrows, David N. et al. (2005). "The Swift X-Ray Telescope". In: *Space Science Reviews* 120.3, pp. 165–195.
- Catanese, M. et al. (1997). "Multiwavelength Observations of a Flare from Markarian 501". In: *The Astrophysical Journal Letters* 487, pp. L143–L146.
- Chakraborty, Nachiketa et al. (2015). "Rapid variability at very high energies in Mrk 501". In: *arXiv:1509.04893 [astro-ph]*.
- Cologna, G. et al. (2015). "Spectral characteristics of Mrk 501 during the 2012 and 2014 flaring states". In: 34th International Cosmic Ray Conference (ICRC2015). Vol. 34. eprint: arXiv:1509.04458, p. 761.
- Connolly, S. et al. (2015). "'Harder when Brighter' Spectral Variability in Low-Luminosity AGN". In: *The Extremes of Black Hole Accretion*. Vol. 1, p. 24.
- Cusumano, G. et al. (2001). "The curved X-ray spectrum of PSR B1509-58 observed with BeppoSAX". In: *A&A* 375.2, pp. 397–404.

- Donato, D. et al. (2001). "Hard X-ray properties of blazars". In: *Astronomy & Astrophysics* 375.3, pp. 739–751.
- Elitzur, Moshe (2006). "The obscuring torus in AGN". In: *New Astronomy Reviews* 50, pp. 728–731.
- Fanaroff, B. L. and J. M. Riley (1974). "The morphology of extragalactic radio sources of high and low luminosity". In: *Monthly Notices of the Royal Astronomical Society* 167, 31P–36P.
- Fath, E. A. (1909). "The Spectra of Some Spiral Nebulæ and Globular Star Clusters". In: *Publications of the Astronomical Society of the Pacific* 21, pp. 138–143.
- Fossati, G. et al. (1998). "A unifying view of the spectral energy distributions of blazars". In: *Monthly Notices of the Royal Astronomical Society* 299, pp. 433–448.
- Gehrels, N. et al. (2004). "The Swift Gamma-Ray Burst Mission". In: *arXiv:astro-ph/0405233* 727, pp. 637–641.
- Ghisellini, Gabriele and Piero Madau (1996). "On the origin of the γ -ray emission in blazars". In: *Monthly Notices of the Royal Astronomical Society* 280.1, pp. 67–76.
- Kalberla, P.M.W. et al. (2005). "The Leiden/Argentine/Bonn (LAB) Survey of Galactic HI. Final data release of the combined LDS and IAR surveys with improved stray-radiation corrections". In: *aap* 440, pp. 775–782.
- Kellermann, K. I. et al. (1989). "VLA observations of objects in the Palomar Bright Quasar Survey". In: *The Astronomical Journal* 98, pp. 1195–1207.
- Kirsch, M. G. et al. (2005). "Crab: the standard x-ray candle with all (modern) x-ray satellites". In: vol. 5898.
- Krolik, Julian Henry (1999). *Active Galactic Nuclei: From the Central Black Hole to the Galactic Environment*. Google-Books-ID: oRK8otMiWlgC. Princeton University Press. 632 pp.
- Laing, Robert A. and Alan H. Bridle (1987). "Rotation measure variation across M84". In: *Monthly Notices of the Royal Astronomical Society* 228, pp. 557–571.
- Mannheim, K. (1993). "The proton blazar". In: *Astronomy and Astrophysics* 269, pp. 67–76.
- Markaryan, B. E. and V. A. Lipovetskii (1972). "Galaxies with ultraviolet continuum V". In: *Astrophysics* 8.2, pp. 89–99.
- Massaro, E. et al. (2004). "Log-parabolic spectra and particle acceleration in the BL Lac object Mkn 421: Spectral analysis of the complete BeppoSAX wide band X-ray data set". In: *Astronomy and Astrophysics* 413, pp. 489–503.
- O'Dell, S. L. et al. (1978). "The changes in spectral-flux distribution during variability of extragalactic nonthermal sources, 0.36 to 3.5 microns." In: *The Astrophysical Journal Supplement Series* 38, pp. 267–286.

- Optical spectra of various kinds of active galactic nuclei*. URL: <http://pages.astronomy.ua.edu/keel/agn/spectra.html>.
- Park, Taeyoung et al. (2006). "Bayesian Estimation of Hardness Ratios: Modeling and Computations". In: *The Astrophysical Journal* 652.1, p. 610.
- Peterson, B. M. et al. (2004). "Central Masses and Broad-Line Region Sizes of Active Galactic Nuclei. II. A Homogeneous Analysis of a Large Reverberation-Mapping Database". In: *The Astrophysical Journal* 613, pp. 682–699.
- Pian, Elena et al. (1998). "BeppoSAX Observations of Unprecedented Synchrotron Activity in the BL Lacertae Object Markarian 501". In: *The Astrophysical Journal Letters* 492.1, p. L17.
- Quinn, J. et al. (1996). "Detection of Gamma Rays with $E > 300$ GeV from Markarian 501". In: *The Astrophysical Journal Letters* 456.2, p. L83.
- Romano, P. et al. (2006). "Panchromatic study of GRB 060124: from precursor to afterglow". In: *Astronomy & Astrophysics* 456.3, pp. 917–927.
- Roming, Peter W. A. et al. (2005). "The Swift Ultra-Violet/Optical Telescope". In: *Space Science Reviews* 120, pp. 95–142.
- Rowan-Robinson, M. (1977). "On the unity of activity in galaxies". In: *The Astrophysical Journal* 213, pp. 635–647.
- Seyfert, Carl K. (1943). "Nuclear Emission in Spiral Nebulae." In: *The Astrophysical Journal* 97, p. 28.
- Swift XRT data*. URL: https://swift.gsfc.nasa.gov/about_swift/xrt_desc.html.
- UKSSDC | *XRT threads*. URL: <http://www.swift.ac.uk/analysis/xrt/pileup.php> (visited on 05/17/2017).
- Urry, C. Megan and Paolo Padovani (1995). "Unified Schemes for Radio-Loud Active Galactic Nuclei". In: *Publications of the Astronomical Society of the Pacific* 107, p. 803.
- Vaucouleurs, G. de et al. (1991). *Third Reference Catalogue of Bright Galaxies. Volume I: Explanations and references. Volume II: Data for galaxies between 0h and 12h. Volume III: Data for galaxies between 12h and 24h.*
- Vaughan, S. et al. (2003). "On characterising the variability properties of X-ray light curves from active galaxies". In: *Monthly Notices of the Royal Astronomical Society* 345.4, pp. 1271–1284.
- Verner, D. A. et al. (1996). "Atomic Data for Astrophysics. II. New Analytic FITS for Photoionization Cross Sections of Atoms and Ions". In: *The Astrophysical Journal* 465, p. 487.
- Vestergaard, Marianne and Bradley M. Peterson (2006). "Determining Central Black Hole Masses in Distant Active Galaxies and Quasars. II. Improved Optical and UV Scaling Relationships". In: *The Astrophysical Journal* 641.2, p. 689.

Weidinger, Matthias, Michael Ruger, and Felix Spanier (2010). "Modelling the steady state spectral energy distribution of the BL-Lac Object PKS 2155-304 using a self-consistent SSC model". In: *Astrophysics and Space Sciences Transactions* 6.1, pp. 1–7.

Wilms, J., A. Allen, and R. McCray (2000). "On the Absorption of X-Rays in the Interstellar Medium". In: *apj* 542, pp. 914–924.

This research has made use of ISIS functions provided by ECAP/Remeis observatory and MIT(<http://www.sternwarte.uni-erlangen.de/isis>). ISIS version: 1.6.2-36

Acknowledgements

My thanks go to:

- Prof. Dr. Matthias Kadler, my supervisor, who was always helpful and provided me with a lot of information and knowledge used in this work. His lectures convinced me to write my Bachelor's Thesis at the Chair for Astronomy.
- Annika Kreikenbohm, for the continuous support and collaboration, who introduced me to the field of X-ray astronomy and was of great help in many ways. She was always available to answer any question, and to help me find and fix problems with my ISIS scripts.
- Katharina Leiter, who helped whenever Annika was not available and gave lots of valuable advice.
- The whole Chair for Astronomy, under the direction of Prof. Dr. Karl Mannheim, for welcoming me with open arms.
- My colleague, friend and office mate Alexander Komenda, who wrote his thesis simultaneously, because of the great work climate in our shared office, as well as the many discussions we had on-, as well as off-topic.
- My family for supporting me throughout the course of my studies, and especially my father for proof reading.
- My girlfriend Noémie for emotional support while I was working on this thesis.

Declaration of Authorship

I, Jonas Sinapius, declare that this thesis titled, "Spectral Analysis of *Swift*-XRT monitoring observations of the blazar Mrk 501" and the work presented in it are my own. I confirm that:

- This work was done wholly or mainly while in candidature for a research degree at this University.
- Where any part of this thesis has previously been submitted for a degree or any other qualification at this University or any other institution, this has been clearly stated.
- Where I have consulted the published work of others, this is always clearly attributed.
- Where I have quoted from the work of others, the source is always given. With the exception of such quotations, this thesis is entirely my own work.
- I have acknowledged all main sources of help.
- Where the thesis is based on work done by myself jointly with others, I have made clear exactly what was done by others and what I have contributed myself.

Signed: _____

JSinapius

Date: 15.07.2017